iScience

CellPress

Article

# Multi-Element Topochemical-Molten Salt Synthesis of One-Dimensional Piezoelectric Perovskite

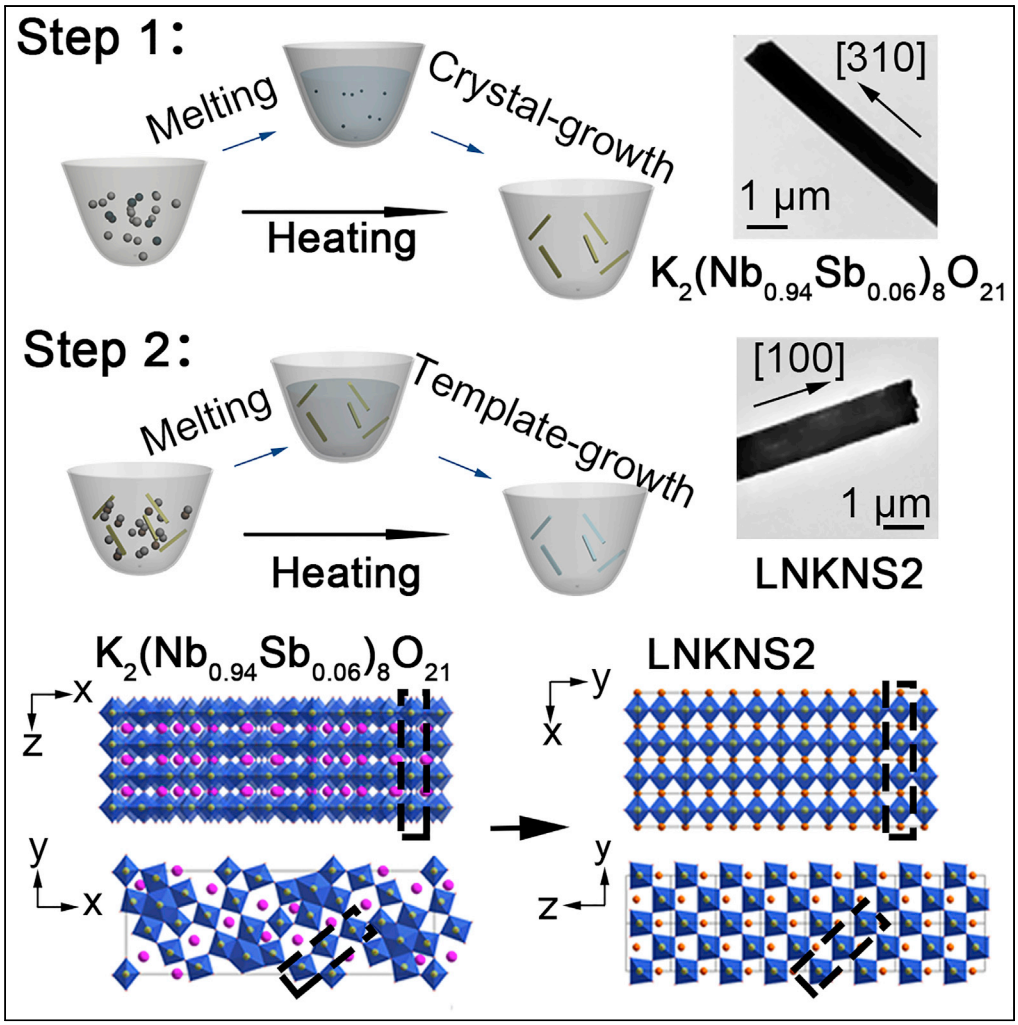


Lihong Li, Zhongyuan Xiang, Meng Gao, ..., Fengyu Li, Xianran Xing, Yanlin Song

ylsong@iccas.ac.cn

## HIGHLIGHTS

A kind of Multi-element Topochemical-Molten Salt method was proposed

Large-scale 1D perovskites with multi-doping of A-sites and B-sites was realized

The formation and structure of the 1D multi-perovskite niobate were clearly deduced

The output voltage of the prepared device was 600% of that of the control sample

Li et al., iScience *17*, 1–9
July 26, 2019 
https://doi.org/10.1016/j.isci.2019.06.012

iScience

CellPress

Article

# Multi-Element Topochemical-Molten Salt Synthesis of One-Dimensional Piezoelectric Perovskite

Lihong Li,[1] Zhongyuan Xiang,[1] Meng Gao,[1] Cheng Bian,[2] Meng Su,[2] Fengyu Li,[1] Xianran Xing,[2] and Yanlin Song[1,3,*]

## SUMMARY

**One-dimensional perovskites are an interesting material for energy and optoelectronic applications. However, exploring the full wealth of architectures these materials could allow, through multi-element doping of A-sites and B-sites, is still a challenge. Here, we report a high-yield synthetic strategy for 1D perovskites via a two-step method based on a multi-element topochemical-molten salt method. Typically, a high yield of 1D multicomponent perovskite niobates $(Li_{0.06}Na_{0.47}K_{0.47})(Nb_{0.94}Sb_{0.06})O_3$ (LNKNS2) is rapidly achieved from as-synthesized 1D $K_2(Nb_{0.94}Sb_{0.06})_8O_{21}$ with multi-element B-sites. In this process, 1D $K_2(Nb_{0.94}Sb_{0.06})_8O_{21}$ has been first achieved, and the proportion of the ions in A-sites is affected by the radius and molar ratio of ions. The z axis direction of $K_2(Nb_{0.94}Sb_{0.06})_8O_{21}$ rod is transformed into the x axis direction of LNKNS2 rod. Furthermore, the output voltage of the 1D niobates-based flexible piezoelectric device (FPD) was nearly 600% compared with that of the isotropic niobates-based FPD. This work also allows convenient fabrication of other 1D multicomponent perovskites.**

## INTRODUCTION

One-dimensional (1D) micro-nanomaterials have fascinated wide interest owing to their 2D confinement structure and exotic mechanical, electrical, and optical properties (You et al., 2017; Ning et al., 2018; Duan et al., 2003; Li et al., 2016; Lee et al., 2017; Niu et al., 2017; Arellano et al., 2018; Lu et al., 2018; Yang et al., 2012a, 2012b, 2012c; Yang et al., 2011). For flexible electronic devices (Deutz et al., 2017; Wang, 2018; Wang et al., 2019; Yang et al., 2012a, 2012b, 2012c), which exhibit great significance for viable economic growth and the enhancement of human quality of life, the 1D materials are highly desirable, and a wide range of 1D materials-based flexible devices such as field-effect transistors (Qing et al., 2014), flexible display devices (Wang et al., 2017), flexible photodetectors (Zhou et al., 2018), flexible sensors (Deutz et al., 2017; Rim et al., 2016), and flexible energy storage devices (Gao et al., 2016; Park et al., 2017; Deng et al., 2018; Guo et al., 2012) have been demonstrated to show superior performance than their counterparts with arbitrary shapes.

Perovskite materials, owing to their applications in piezoelectric, ferroelectric, solar cells, and other fields, arouse a research boom (Burschka et al., 2013; Abdi-Jalebi et al., 2018; Becker et al., 2018; Christians et al., 2018; Domanski et al., 2018; Zhang et al., 2018a, 2018b; Yang et al., 2019; Wu et al., 2012a, 2012b). The structure of perovskite materials is mainly $ABO_3$-type of cubic or pseudo cubic phase. Generally, the shape of crystalline particles depends on their intrinsic structure, which means that materials with cubic phase usually form isotropic particles (Pribosic et al., 2005). Meanwhile, owing to the demand for various properties, A-sites and B-sites of perovskites are doped with multi-elements mainly via solid-state method (Zheng et al., 2018; Wu et al., 2016; Qin et al., 2016; Li et al., 2018; Liu et al., 2018). 1D perovskites materials, because of their unique electronic, nonlinear optical probe and mechanical properties, have potential in various fields (Ren et al., 2010; Nakayama et al., 2007; Gao et al., 2018; Yang et al., 2012a, 2012b, 2012c; Wu et al., 2012a, 2012b). To further improve performance, it is critical to achieve 1D multi-perovskite materials, which can incorporate 1D structural design into perovskites (Zhai et al., 2018; Sun et al., 2016; Meng et al., 2017; Li et al., 2009; Cheng et al., 2013); however, the preparation of 1D perovskites with multi-doping of A-sites and B-sites at large scale is still a great challenge. At present, only a few synthesis methods of 1D $ABO_3$ perovskites are reported, which mainly focus on the preparation of A-sites or B-sites as a single element, such as solvothermal method (Zhai et al., 2018), hydrothermal method (Nakayama et al., 2007), reprecipitation method (Sun et al., 2016), sol-gel method (Meng et al., 2017),

[1]Key Laboratory of Green Printing, Institute of Chemistry, Chinese Academy of Sciences (ICCAS), Beijing Engineering Research Center of Nanomaterials for Green Printing Technology, Beijing National Laboratory for Molecular Sciences (BNLMS), Beijing 100190, P. R. China

[2]Department of Physical Chemistry and State Key Laboratory for Advanced Metals and Materials, University of Science and Technology Beijing, Beijing 100083, China

[3]Lead Contact

*Correspondence: ylsong@iccas.ac.cn

https://doi.org/10.1016/j.isci.2019.06.012

  

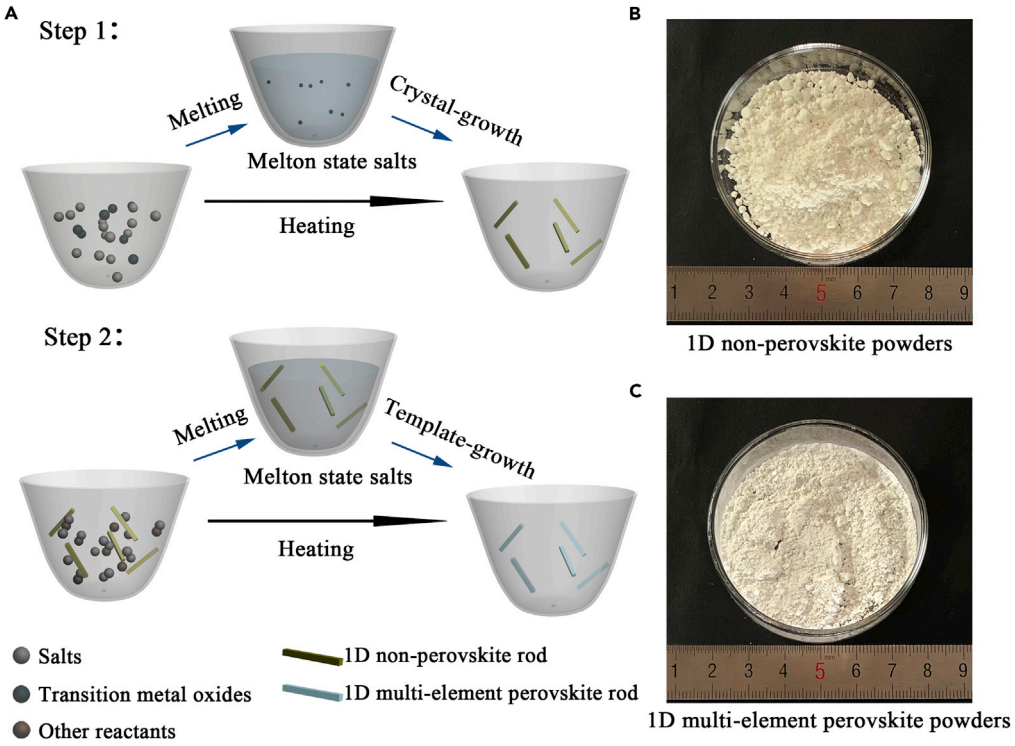


**Figure 1. Synthesis Scheme of 1D Multi-Perovskite via Two Steps of Multi-Element Topochemical-Molten Salt Method**

(A) Schematic of the MTMS synthesis of 1D multi-perovskite.

(B) Image of 1D $K_2(Nb_{0.94}Sb_{0.06})_8O_{21}$ powder with large scale after one time synthesis of first step (see also Figure S1).

(C) Image of 1D $(Li_{0.06}Na_{0.47}K_{0.47})(Nb_{0.94}Sb_{0.06})O_3$ powder with large scale after one time preparation (see also Figure S2).

See also Figures S1 and S2.

and molten salt method (Li et al., 2009; Cheng et al., 2013), whereas it is difficult to control the multi-component composition of perovskites at A-sites and B-sites with these methods.

Perovskite niobate is considered as one of the most competitive lead-free materials to replace lead-bearing perovskite because of its excellent piezoelectric and ferroelectric properties and suitable Curie temperature (Saito et al., 2004; Zhang et al., 2018a, 2018b; Xu et al., 2016). Herein, we proposed a simple two-step method to synthesize 1D perovskite-type niobate based on a kind of Multi-element Topochemical-Molten Salt (MTMS) method. The key to this approach was that, using 1D anisotropic non-perovskite-type niobate with multi-"B-sites" element as template, large quantities of 1D morphology of perovskite materials at the boundary of quasi-isomorphic phase with controlling multi-doping A-sites and B-sites could be achieved. Accordingly, for the first time, we synthesized the rod-like $K_2(Nb_{0.94}Sb_{0.06})_8O_{21}$ and proposed the mechanism of its derivation into perovskite-type multicomponent niobate products. Furthermore, flexible piezoelectric device (FPD) with planar orientation of rod-like product was prepared. At the same degree of bending, the output voltage was nearly 600% compared with that of the granular material of similar component. This strategy could be extended to the synthesis of large-scale other 1D multi-perovskite materials, which were expected to be widely used in flexible electronics, sensor devices, and energy storage.

## RESULTS AND DISCUSSION

The two-step strategy was processed to synthesize 1D multi-perovskite as shown in Figure 1A. Salts were common ionic crystals that could ionize in the molten state. First, salts mixed with a certain proportion of transition metal oxides and 1D anisotropic non-perovskite-type oxides with multi-"B-sites" element was rapidly synthesized via its intrinsic crystal growth in molten salts, and large scale of anisotropic non-perovskite-type oxides was obtained (Figure 1B). Then 1D and multi-dimensional $ABO_3$ perovskite oxides could

be synthesized in large quantities (Figure 1C) by using the anisotropic non-perovskite-type oxides as template, mixed with other reactors and salts, via the MTMS method. The MTMS method is a kind of the multi-element, environmentally friendly, and mild way to prepare pure and morphologically controllable samples at a moderate temperature in a short soaking time, and it is developed from the molten salt method. The morphology of the products can inherit that of the major solid-state raw materials via the MTMS method, that is, the shape and size of the as-synthesized compounds can be controlled by an appropriate choice of raw materials, salts, sintering temperature, and reaction time. The MTMS method has the advantage of combining the molten salt method and the topochemical method, associated with the use of localized solid-state compound transformations via the exchange, deletion, or insertion of different individual ions. In the typical experiment, the non-perovskite-type niobate $K_2(Nb_{0.94}Sb_{0.06})_8O_{21}$ rods with multi-"B-sites" was prepared by calcinations of corresponding mole ratio of $Nb_2O_5$ and $Sb_2O_3$ in equal weight molten KCl salts at 1,000°C for 3 h. The composition could be confirmed by the energy dispersive spectrometry (EDX) pattern (Figure S1), and the reaction could be as follows.

$$3.76Nb_2O_5 + 0.24Sb_2O_3 + 2KCl + 0.74O_2 \xrightarrow[Na_2CO_3]{KCl} K_2(Nb_{0.94}Sb_{0.06})_8O_{21} + Cl_2\uparrow \qquad \text{(Equation 1)}$$

Then, the multi-niobate $(Li_{0.06}Na_xK_{0.94-x})(Nb_{0.94}Sb_{0.06})O_3$, marked as LNKNS*m*, was synthesized from an MTMS reaction by mixing the 0.25 mol $K_2(Nb_{0.94}Sb_{0.06})_8O_{21}$ rods and 0.06 mol $Li_2CO_3$ with different amounts of $Na_2CO_3$ (*m* mol = 0.5, 1, 1.5, 2, and 2.5 mol) soaked in KCl melts at 800°C for 100 min. The resulting powders were washed several times with distilled water and then dried at 80°C. *x* is the amount of $Na^+$ ions in LNKNS*m*. The reaction involving the LNKNS*m* formation was proposed as follows.

$$0.25K_2(Nb_{0.94}Sb_{0.06})_8O_{21} + xNa_2CO_3 + 0.06Li_2CO_3 + (1.38-2x)KCl + (0.94-x)O_2 \qquad \text{(Equation 2)}$$
$$\xrightarrow[Na_2CO_3]{KCl} 2(Li_{0.06}Na_xK_{0.94-x})(Nb_{0.94}Sb_{0.06})O_3 + (0.69-x)\ Cl_2\uparrow$$

In Equation 2, KCl salt took part in the reaction and the $K^+$ ions (radius: 1.33 Å) mainly competed with $Na^+$ ions (radius: 1.02 Å) to occupy the A-sites of LNKNS*m* but had almost no effect on $Li^+$ ion (radius: 0.76 Å). This phenomenon might be caused by their different radii and could be confirmed by the X-ray diffraction (XRD) patterns, EDX patterns, and inductively coupled plasma (ICP) measurements of LNKNS*m* with different value of *m* (Figures 2A and S2, and Table S1). XRD patterns of LNKNS*m* indicated the phase evolution with the change of *m*. Table S2 listed the crystal structure and the lattice parameters of LNKNS*m* indexed from the XRD patterns. LNKNS0.5, LNKNS1, and LNKNS1.5 were indexed in an orthorhombic symmetry (space group *Amm*2), LNKNS2 ($(Li_{0.06}Na_{0.47}K_{0.47})(Nb_{0.94}Sb_{0.06})O_3$) was indexed in double phases with different orthorhombic symmetries (space groups *Amm*2 and *Pmmm*), and LNKNS2.5 was indexed in an orthorhombic symmetry (space group *Pmmm*). From the lattice parameter changes of the orthorhombic, it could be found that the substitution of some of the $Na^+$ for $K^+$ results in decreasing lattice constants, since the ionic radius of $K^+$ was much larger than that of $Na^+$. A phase transition of LNKNS*m* occurs from an orthorhombic phase (*Amm*2) to another orthorhombic phase (*Pmmm*) with an increase in the Na content. It was likely that there was a morphotropic phase boundary (MPB), at which the property of the material could be enhanced largely (Saito et al., 2004), near *m* = 2 for LNKNS*m*.

For further analysis of the detailed structural evolution, the atomic structures of $K_2(Nb_{0.94}Sb_{0.06})_8O_{21}$ and LNKNS2 were calculated and discussed. Figure 2B showed the XRD pattern of the as-synthesized non-perovskite $K_2(Nb_{0.94}Sb_{0.06})_8O_{21}$, indicating pure phase of the product. The XRD Rietveld method with FULLPROF Suite software package was used to refine the structure, and the phase of $K_2(Nb_{0.94}Sb_{0.06})_8O_{21}$ was orthorhombic (*Pbam*) with lattice parameters of a = 37.498 Å, b = 12.509 Å, and c = 3.963 Å, which had similar structure of $K_2Nb_8O_{21}$ phase (JCPDS 76–977). The detailed structure and atomic parameters of the $K_2(Nb_{0.94}Sb_{0.06})_8O_{21}$ crystal were shown in Tables S3 and S4 and Data S1 file in Supplemental Information, and the CIF and HKL documents of the $K_2(Nb_{0.94}Sb_{0.06})_8O_{21}$ crystal was deposited with the deposition number CSD 1914187.

Meanwhile, for further clarification, the Rietveld refinement was done for LNKNS2 with a single (space group *Amm*2) (Figure S3) and double phase (space groups *Amm*2 and *Pmmm*) (Figure 2C). From the better fit of the double phase, compared with that of single phase, it revealed that LNKNS2 was in double phases with different orthorhombic symmetries (*Amm*2 and *Pmmm*), and it was confirmed that LNKNS2 was near the MPB. The detailed crystal cell data, atomic parameters, and crystal plane parameters of LNKNS2 with double phase were shown in Tables S5–S7, respectively, the Data S2 file of the LNKNS2 structure was shown

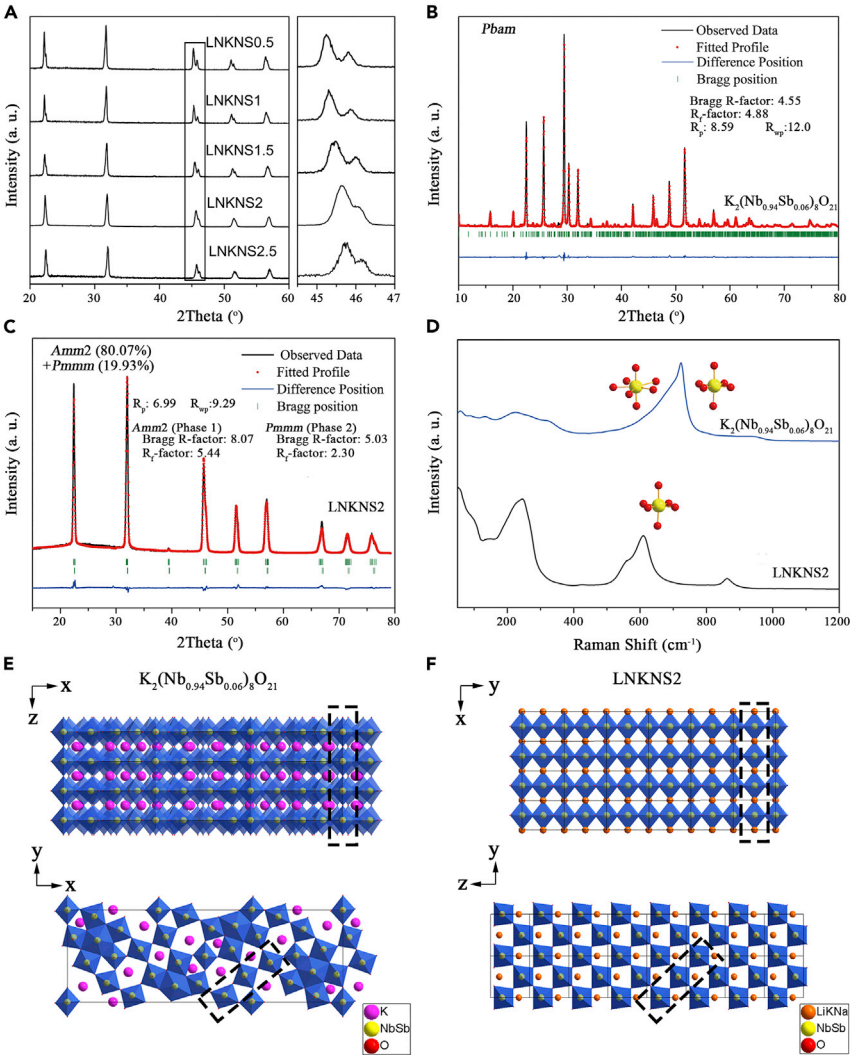


**Figure 2. Structure of the Non-perovskite Niobate and Perovskite Niobate**

(A) X-ray diffractograms of the perovskite niobates LNKNS*m* [*m* = 0.5, 1.0, 1.5, 2.0, 2.5] (see also Figure S2, Tables S1 and S2).

(B) Rietveld refinement profiles for first-step synthesized non-perovskite niobate $K_2(Nb_{0.94}Sb_{0.06})_8O_{21}$. Data were refined in the space group *Pbam*.

(C) Rietveld refinement profiles for the second-step synthesized perovskite niobates $(Li_{0.06}Na_{0.47}K_{0.47})(Nb_{0.94}Sb_{0.06})O_3$ (LNKNS2). Data were refined in double space groups *Amm*2 and *Pmmm* (for data refined in single space group *Amm*2, see also Figure S3).

(D) Raman spectra of $K_2(Nb_{0.94}Sb_{0.06})_8O_{21}$ and LNKNS2.

(E) Crystal structure of atomic structure of $K_2(Nb_{0.94}Sb_{0.06})_8O_{21}$ (see also Tables S3 and S4 and Data S1).

(F) Crystal structure of atomic structure of LNKNS2 (see also Tables S5–S7 and Data S2).

See also Figures S2 and S3, Tables S1–S7, Data S1 and S2.

in Supplemental Information, and the CIF and HKL documents of the $(Li_{0.06}Na_{0.47}K_{0.47})(Nb_{0.94}Sb_{0.06})O_3$ crystal was deposited with the deposition number CSD 1915240.

The structures of $K_2(Nb_{0.94}Sb_{0.06})_8O_{21}$ and LNKNS2 are shown in Figures 2E and 2F, respectively. Both the rods of $K_2(Nb_{0.94}Sb_{0.06})_8O_{21}$ and LNKNS2 had a similar structure of $NbO_6$ octahedron, which shared corners in the *z* axis direction for $K_2(Nb_{0.94}Sb_{0.06})_8O_{21}$ and in the *x* axis direction for $(Li_{0.06}Na_xK_{0.94-x})(Nb_{0.94}Sb_{0.06})O_3$ shown in the oblong loop. For the template of $K_2(Nb_{0.94}Sb_{0.06})_8O_{21}$, the $NbO_7$ decahedron and $NbO_6$ octahedron shared with edges and $NbO_6$ octahedron shared with corners in the *xy* plane. It only required part

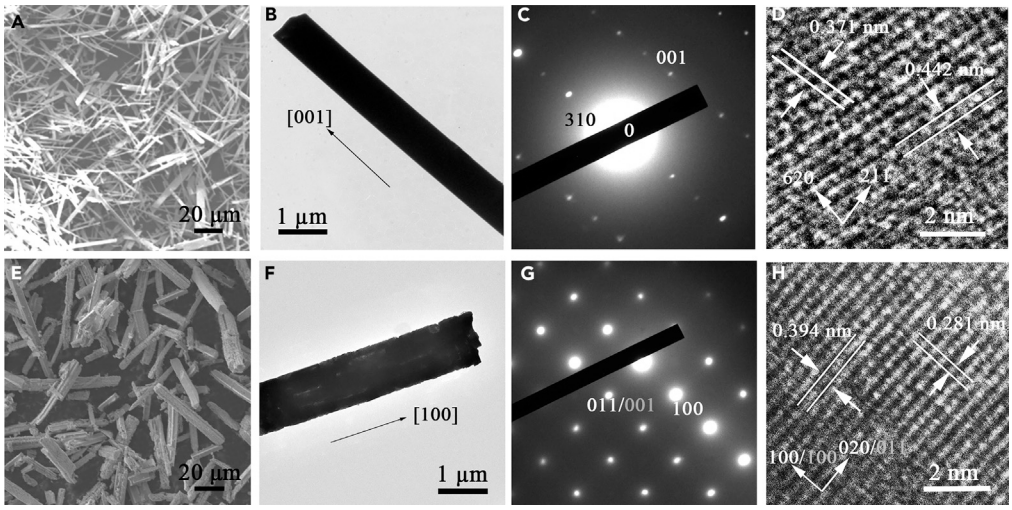


**Figure 3. Morphology of the Non-perovskite Niobate $K_2(Nb_{0.94}Sb_{0.06})_8O_{21}$ and Perovskite Niobate LNKNS2**

(A) The SEM image of the $K_2(Nb_{0.94}Sb_{0.06})_8O_{21}$ rods.

(B) The TEM image of a $K_2(Nb_{0.94}Sb_{0.06})_8O_{21}$ rod along the [001] direction.

(C) The SEAD pattern and the crystal plane data of the diffraction point are determined.

(D) The HRTEM image confirmed the growth direction of the rod.

(E) The SEM image of LNKNS2 rods.

(F) The TEM image of an LNKNS2 rod along the [100] direction.

(G) The SEAD pattern and the crystal plane data of the diffraction point are determined by calculation.

(H) The HRTEM image confirmed the growth direction of the LNKNS2 rod.

of Nb-O bonds breaking and recombination via the entrance of A-sites ions to form the perovskite structure of LNKNS2 with only corner-sharing $NbO_6$ octahedron in the *yz* plane. The similar structure of $NbO_6$ octahedron share with corners was also found in the oblong loop in the *xy* plane of $K_2(Nb_{0.94}Sb_{0.06})_8O_{21}$ and the *yz* plane of LNKNS2. From the above-mentioned analysis, it could be speculated that the *z* axis direction and *xy* plane of $K_2(Nb_{0.94}Sb_{0.06})_8O_{21}$ were transformed into the *x* axis direction and *yz* plane of LNKNS2, respectively. The structural evolution was further confirmed by the Raman patterns of $K_2(Nb_{0.94}Sb_{0.06})_8O_{21}$ and LNKNS2 (Figure 2D). The bands observed in the 700–1,000 $cm^{-1}$ region correspond to the longitudinal optical modes of the Nb-O stretching associated with $NbO_6$ octahedra. The corresponding transverse optical modes were observed around the 650 $cm^{-1}$ regions. The weak bands observed in the 350–560 $cm^{-1}$ region were attributed to be the $T_{2g}$ mode. The strong peaks observed in the range 200–300 $cm^{-1}$ were assigned to the $T_{2u}$ modes. The major band at 700 $cm^{-1}$ of $K_2(Nb_{0.94}Sb_{0.06})_8O_{21}$ was the characteristic band for the structure consisting of $NbO_6$ and $NbO_7$ octahedra-sharing corners (Blasse and Vandenhe, 1972). All of these results were in agreement with the earlier analysis and calculation of the structure $K_2(Nb_{0.94}Sb_{0.06})_8O_{21}$ and LNKNS2.

The morphology of the as-synthesized template of $K_2(Nb_{0.94}Sb_{0.06})_8O_{21}$ rods was examined by scanning electron microscopy (SEM) image, as shown in Figure 3A. A large quantity of rods with diameters of several hundred nanometers and length of several tens of micrometers were observed. The selected area electron diffraction (SAED) patterns taken from the rod of $K_2(Nb_{0.94}Sb_{0.06})_8O_{21}$ (Figures 3B and 3C) indicated that they were single-crystalline in nature. It was further proved by HRTEM image of the same rod (Figure 3D), and the growth direction of the rods was determined to be along [001]. Meanwhile, the 1D structure of LNKNS2 could be maintained from $K_2(Nb_{0.94}Sb_{0.06})_8O_{21}$ rods via the MTMS method shown in the SEM and transmission electron microscopy (TEM) (Figures 3E and 3F). The SAED pattern (Figure 3G) taken from the LNKNS2 rod depicted the single-crystalline nature of the obtained perovskite niobate via the MTMS method, which was also proved by HRTEM image of the same rod (Figure 3H). The growth direction of LNKNS2 rods was determined to be along [100], which was also consistent with the earlier speculation of the structural transformation, that is, *z* axis direction of $K_2(Nb_{0.94}Sb_{0.06})_8O_{21}$ was transformed into the *x* axis direction of LNKNS2. The two-step MTMS strategy could be a general method to synthesize a wide range of 1D multi-perovskites, including other multi-perovskite niobate materials with high electric properties (Table 1), which used to be isotropy shape synthesized by the solid-state method (Wu et al., 2016; Hao

| Morphology of the Compositions | This Work[a] | Previous Work |
|---|---|---|
| $0.96[0.93(K_{0.5}Na_{0.5})NbO_3\text{-}0.07LiNbO_3]\text{-}0.04CaZrO_3$ | 1D rods[a] | Isotropic particles (Zhang et al., 2015) |
| $0.9625(K_{0.48}Na_{0.52})(Nb_{0.94}Sb_{0.06})O_3\text{-}0.0375Bi_{0.5}(Na_{0.82}K_{0.18})_{0.5}ZrO_3$ | 1D rods[a] | Isotropic particles (Qin et al., 2016) |
| $0.96(K_{0.48}Na_{0.52})(Nb_{0.95}Sb_{0.05})O_3\text{-}0.04Bi_{0.5}Na_{0.5}ZrO_3$ | 1D rods[a] | Isotropic particles (Zheng et al., 2015) |
| $0.9625(K_{0.45}Na_{0.55})(Nb_{0.96}Sb_{0.04})O_3\text{-}0.0375Bi_{0.5}Na_{0.5}Zr_{0.85}Hf_{0.15}O_3$ | 1D rods[a] | Isotropic particles (Tao and Wu, 2016) |
| $0.964(K_{0.4}Na_{0.6})\ (Nb_{0.955}Sb_{0.045})O_3\text{-}0.006BiFeO_3\text{-}0.03Bi_{0.5}Na_{0.5}ZrO_3$ | 1D rods[a] | Isotropic particles (Wu et al., 2016) |

**Table 1. Morphology and Structure of Some Multi-Perovskite Niobate Materials**

More details in Figures S4 and S5.

This work via the MTMS method, and previous work via the solid-state method.

[a]The XRD patterns, SEM images, and EDX data of the compositions have been supplied in Figures S4 and S5.

et al., 2019). The XRD patterns, SEM images, and EDX data of these multi-perovskite niobate rods have been supplied in Figures S4 and S5.

To further reveal the property of the as-synthesis perovskite niobate rods, the LNKNS2 rods-based FPD (LNKNS2-FPD) was prepared. The schematic fabrication process of LNKNS2-FPD is shown in Figure S6 (detailed information is given in the Transparent Methods supplemental file). Figure 4A demonstrated the cross-sectional SEM image of the film of LNKNS2 rods with the poly(dimethylsiloxane) (PDMS) matrix via spin-coating, and a magnified cross-sectional SEM image (Figure 4B) showed that the LNKNS2 rods adopt preferential orientations in PDMS. The output of the FPD during the periodic bending/unbending tests was carried out, employing a bending stage executed at a horizontal displacement of 2 cm with a moving speed of one-side movable fixture of 30 mm/s (see Video S1). Figure 4C showed that the output of open-circuit voltage of the LNKNS2-FPD was 600% compared with that of FPD with the isotropic niobates (I-LNKNS-FPD), which had a similar composition $[(Li_{0.06}Na_{0.47}K_{0.47})(Nb_{0.94}Sb_{0.06})O_3]$ obtained via the solid-state method, for the same bending angle. The XRD pattern, SEM images, and EDX image of the isotropic niobates are shown in Figures S7–S9, respectively. It was interesting that the output voltage of the FPD was remarkably enhanced. The voltage generated by the FPD, $V_{out}$, could be calculated from the Equation 3 (Xu et al., 2013; Hwang et al., 2014).

$$V_{out} = \int g_{33} \cdot \varepsilon(l) \cdot Y dl \qquad \text{(Equation 3)}$$

where $l$ is the perpendicular distance between the adjacent electrodes, $\varepsilon(l)$ is the function of the strain along the direction of $l$, Y is the Young's modulus, and $g_{33}$ is the piezoelectric voltage coefficient. Accordingly, the first merit of LNKNS2 rods-based FPD for piezoelectric applications was their high piezoelectric constant ($d_{33}$ = 340 pC/N), which increases near 25% of that obtained from isotropic niobates prepared in this work ($d_{33}$ = 270 pC/N) and that of regular particles with similar composition synthesized via the solid-state method reported in previous study ($d_{33}$ = 267 pC/N) (Zang et al., 2006). So, the piezoelectric constant corresponded to a high $g_{33}$ following $g_{33} = d_{33}/\varepsilon_0 \cdot K$, where $\varepsilon_0$ was the permittivity of free space and K was the relative dielectric constant of the FPD. Meanwhile, the high anisotropic LNKNS2 rods along [100] made the FPD a little textured (Figure 4B), and the identity of the nanowires' longitudinal direction led to an enlargement of the nanowires' deformation (Deutz et al., 2017; Chen et al., 2017), thus resulting in exaggerated dipole displacement and piezoelectric property. For further clarification, a corresponding simulation was carried out via a finite element method, and the numerical modeling result was approximately in agreement with the experimental result. The calculated output of open-circuit voltage of the LNKNS2-FPD and I-LNKNS-FPD was presented in Figure 4D, where piezopotential was depicted by color code. Furthermore, to investigate the effect of the ratio of length to width of the perovskite-type niobates, the niobates (S-LNKNS2) rods with short length were achieved by reducing the amount of salt in first step via the MTMS method (see Figures S10–S12, and Transparent Methods), and the statistical data on the ratio between length and width of the LNKNS2, S-LNKNS, and I-LNKNS were about 1:1, 1:6, and 1:12, respectively. The output of the FPD with S-LNKNS was obtained under the same test condition of LNKNS2-FPD and I-LNKNS-FPD (see Figure S13). It was found that, with the increasing ratio between length and width, the open circuit voltage of the FPD increases. The simulation of piezoelectric voltage output of FPD with particles of different ratios of length to width (1:1, 1:6, and 1:12) was also provided (see Figure S14), which was consistent with the experimental result. Meanwhile, Figure S15 exhibited the clear increase of the

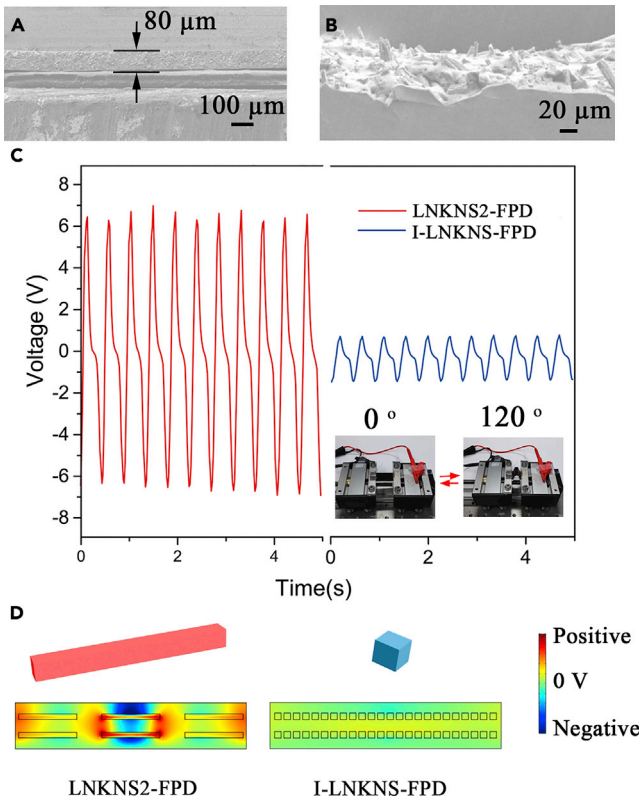


**Figure 4. The Electric Properties of FPD Based on the As-synthesis Perovskite Niobate Rods**

(A) Cross-sectional SEM image of the LNKNS2 rods/PDMS film.

(B) Magnified cross-sectional SEM photograph of the LNKNS2 rods/PDMS film.

(C) The measured open-circuit voltage of an LNKNS2-FPD and I-LNKNS-FPD. The insets are optical images of an FPD in its bending and releasing states.

(D) Simulation results of voltage output of an LNKNS2-FPD and an I-LNKNS-FPD.

Also see Figures S6–S15 and Video S1.

output voltage of the LNKNS2-FPD with increasing bending angle. This property is of benefit in the wearable area and other fields.

In summary, we proposed a strategy based on MTMS method to achieve large-scale 1D perovskite materials with controlling multi-doping A-sites and B-sites. The formation, structural evolution, quality, and scalability of the 1D multi-perovskite niobate LNKNS2 were clearly highlighted. The z axis direction and xy plane of $K_2(Nb_{0.94}Sb_{0.06})_8O_{21}$ were transformed into the x axis direction and yz plane of LNKNS2, respectively. The piezoelectric constant ($d_{33}$) of LNKNS2 increases near 25% of that obtained from the isotropic particles. The output of open-circuit voltage of the LNKNS2-FPD is 600% of that of the I-LNKNS-FPD. Furthermore, the two-step MTMS strategy can be applied generally to a wide range of 1D multi-perovskites, including multi-perovskite niobate materials with high electric properties, to establish a library of 1D multi-perovskites with diverse functionalities. Our study thus provides a robust pathway to the scalable production of 1D multi-perovskites for electronics, piezoelectrics, self-generating, and energy-related fields.

## METHODS

All methods can be found in the accompanying Transparent Methods supplemental file.

## DATA AND SOFTWARE AVAILABILITY

The Accession Numbers for the crystallographic entries deposited in the CCDC database: CSD 1914187 for $K_2(Nb_{0.94}Sb_{0.06})_8O_{21}$ crystal and CSD 1915240 for $(Li_{0.06}Na_{0.47}K_{0.47})(Nb_{0.94}Sb_{0.06})O_3$.

## SUPPLEMENTAL INFORMATION

Supplemental Information can be found online at https://doi.org/10.1016/j.isci.2019.06.012.

## ACKNOWLEDGMENTS

The authors thank the financial support of the National Natural Science Foundation of China (Grant Nos. 21875260, 21671193, 51773206, 21590793, 21731001, 51803217), the Tianjin Nature Science Foundation (Grant Nos. 18JCQNJC76800), the National Key R&D Program of China (Grant Nos. 2018YFA0208501, 2016YFC1100502, 2016YFB0401603, and 2016YFB0401100), the External Cooperation Program of BIC, Chinese Academy of Sciences, Grant No. GJHZ201948, the "Research Plan Program" of Tianjin Municipal Education Commission (Grant No. 2018KJ095), and the Chinese Academy of Sciences and K. C. Wong Education Foundation.

## AUTHOR CONTRIBUTIONS

L.L., Z.X., and C.B. performed the synthesis, measurements, and characterizations. L.L., M.G., and M.S. performed the calculation. L.L., Y.S., F.L., and X.X. analyzed the data. L.L. wrote the original draft. L.L., Y.S., and X.X. revised the manuscript.

## DECLARATION OF INTERESTS

The authors declare no competing interests.

Received: March 4, 2019
Revised: May 15, 2019
Accepted: June 6, 2019
Published: July 26, 2019

## REFERENCES

Abdi-Jalebi, M., Andaji-Garmaroudi, Z., Cacovich, S., Stavrakas, C., Philippe, B., Richter, J.M., Alsari, M., Booker, E.P., Hutter, E.M., Pearson, A.J., et al. (2018). Maximizing and stabilizing luminescence from halide perovskites with potassium passivation. Nature *555*, 497–501.

Arellano, D.L.G., Burnett, E.K., Uzun, S.D., Zakashansky, J.A., Champagne, V.K., III, George, M., Mannsfeld, S.C.B., and Briseno, A.L. (2018). Phase transition of graphene-templated vertical zinc phthalocyanine nanopillars. J. Am. Chem. Soc. *140*, 8185–8191.

Becker, M.A., Vaxenburg, R., Nedelcu, G., Sercel, P.C., Shabaev, A., Mehl, M.J., Michopoulos, J.G., Lambrakos, S.G., Bernstein, N., Lyons, J.L., et al. (2018). Bright triplet excitons in caesium lead halide perovskites. Nature *553*, 189–193.

Blasse, G., and Vandenhe, G.P. (1972). Vibrational and electronic-spectra and crystal-structure of cubic $Na_3NbO_4$. Mater. Res. Bull. *7*, 1041–1043.

Burschka, J., Pellet, N., Moon, S.-J., Humphry-Baker, R., Gao, P., Nazeeruddin, M.K., and Graetzel, M. (2013). Sequential deposition as a route to high-performance perovskite-sensitized solar cells. Nature *499*, 316–319.

Chen, Z., Wang, Z., Li, X., Lin, Y., Luo, N., Long, M., Zhao, N., and Xu, J.-B. (2017). Flexible piezoelectric-induced pressure sensors for static measurements based on nanowires/graphene heterostructures. ACS Nano *11*, 4507–4513.

Cheng, L.-Q., Wang, K., and Li, J.-F. (2013). Synthesis of highly piezoelectric lead-free (K, Na) NbO3 one-dimensional perovskite nanostructures. Chem. Commun. (Camb.) *49*, 4003–4005.

Christians, J.A., Schulz, P., Tinkham, J.S., Schloemer, T.H., Harvey, S.P., de Villers, B.J.T., Sellinger, A., Berry, J.J., and Luther, J.M. (2018). Tailored interfaces of unencapsulated perovskite solar cells for > 1,000 hour operational stability. Nat. Energy *3*, 68–74.

Deng, B.H., Lei, T.Y., Zhu, W.H., Xiao, L., and Liu, J.P. (2018). In-Plane Assembled orthorhombic $Nb_2O_5$ nanorod films with high-rate Li+ intercalation for high-performance flexible Li-ion capacitors. Adv. Funct. Mater. *28*, 1704330.

Deutz, D.B., Mascarenhas, N.T., Schelen, J.B.J., de Leeuw, D.M., van der Zwaag, S., and Groen, P. (2017). Flexible piezoelectric touch sensor by alignment of lead-free alkaline niobate microcubes in PDMS. Adv. Funct. Mater. *27*, 1700728.

Domanski, K., Alharbi, E.A., Hagfeldt, A., Gratzel, M., and Tress, W. (2018). Systematic investigation of the impact of operation conditions on the degradation behaviour of perovskite solar cells. Nat. Energy *3*, 61–67.

Duan, X.F., Huang, Y., Agarwal, R., and Lieber, C.M. (2003). Single-nanowire electrically driven lasers. Nature *421*, 241–245.

Gao, M., Li, L., Li, W., Zhou, H., and Song, Y. (2016). Direct writing of patterned, lead-free nanowire aligned flexible piezoelectric device. Adv. Sci. *3*, 1600120.

Gao, Y., Zhao, L., Shang, Q., Zhong, Y., Liu, Z., Chen, J., Zhang, Z., Shi, J., Du, W., Zhang, Y., et al. (2018). Ultrathin $CsPbX_3$ nanowire arrays with strong emission anisotropy. Adv. Mater. *30*, 1801805.

Guo, W., Xu, C., Wang, X., Wang, S., Pan, C., Lin, C., and Wang, Z.L. (2012). Rectangular bunched rutile $TiO_2$ nanorod arrays grown on carbon fiber for dye-sensitized solar cells. J. Am. Chem. Soc. *134*, 4437–4441.

Hao, J., Li, W., Zhai, J., and Chen, H. (2019). Progress in high-strain perovskite piezoelectric ceramics. Mater. Sci. Eng. R. Rep. *135*, 1–57.

Hwang, G.-T., Park, H., Lee, J.-H., Oh, S., Park, K.-I., Byun, M., Park, H., Ahn, G., Jeong, C.K., No, K., et al. (2014). Self-powered cardiac pacemaker enabled by flexible single crystalline PMN-PT piezoelectric energy harvester. Adv. Mater. *26*, 4880–4887.

Lee, J., Sin, D.H., Moon, B., Shin, J., Kim, H.G., Kim, M., and Cho, K. (2017). Highly crystalline low-bandgap polymer nanowires towards high-performance thick-film organic solar cells exceeding 10% power conversion efficiency. Energy Environ. Sci. *10*, 247–257.

Li, L., Deng, J., Chen, J., Sun, X., Yu, R., Liu, G., and Xing, X. (2009). Wire structure and morphology transformation of niobium oxide and niobates by molten salt synthesis. Chem. Mater. *21*, 1207–1213.

Li, M., Zhao, Z., Cheng, T., Fortunelli, A., Chen, C.-Y., Yu, R., Zhang, Q., Gu, L., Merinov, B.V., Lin, Z., et al. (2016). Ultrafine jagged platinum nanowires enable ultrahigh mass activity for the oxygen reduction reaction. Science *354*, 1414–1419.

Li, P., Zhai, J., Shen, B., Zhang, S., Li, X., Zhu, F., and Zhang, X. (2018). Ultrahigh piezoelectric properties in textured (K,Na)$NbO_3$-based lead-free ceramics. Adv. Mater. *30*, 1705171.

Liu, Q., Zhang, Y., Gao, J., Zhou, Z., Wang, H., Wang, K., Zhang, X., Li, L., and Li, J.-F. (2018). High-performance lead-free piezoelectrics with local structural heterogeneity. Energy Environ. Sci. *11*, 3531–3539.

Lu, J., Xu, C., Li, F., Yang, Z., Peng, Y., Li, X., Que, M., Pan, C., and Wang, Z.L. (2018). Piezoelectric effect tuning on ZnO microwire whispering-gallery mode lasing. ACS Nano *12*, 11899–11906.

Meng, X.H., Wang, W., Ke, H., Rao, J.C., Jia, D.C., and Zhou, Y. (2017). Synthesis, piezoelectric property and domain behaviour of the vertically aligned $K_{1-x}Na_xNbO_3$ nanowire with a morphotropic phase boundary. J. Mater. Chem. C *5*, 747–753.

Nakayama, Y., Pauzauskie, P.J., Radenovic, A., Onorato, R.M., Saykally, R.J., Liphardt, J., and Yang, P. (2007). Tunable nanowire nonlinear optical probe. Nature *447*, 1098.

Ning, J.J., Liu, J., Levi-Kalisman, Y., Frenkel, A.I., and Banin, U. (2018). Controlling anisotropic growth of colloidal ZnSe nanostructures. J. Am. Chem. Soc. *140*, 14627–14637.

Niu, Z.G., Cui, F., Yu, Y., Becknell, N., Sun, Y.C., Khanarian, G., Kim, D., Dou, L., Dehestani, A., Schierle-Arndt, K., et al. (2017). Ultrathin epitaxial Cu@Au core-shell nanowires for stable transparent conductors. J. Am. Chem. Soc. *139*, 7348–7354.

Park, J.H., Hwang, G.-T., Kim, S., Seo, J., Park, H.-J., Yu, K., Kim, T.-S., and Lee, K.J. (2017). Flash-induced self-limited plasmonic welding of silver nanowire network for transparent flexible energy harvester. Adv. Mater. *29*, 1603473.

Pribosic, I., Makovec, D., and Drofenik, M. (2005). Formation of nanoneedles and nanoplatelets of $KNbO_3$ perovskite during templated crystallization of the precursor gel. Chem. Mater. *17*, 2953–2958.

Qin, Y., Zhang, J., Yao, W., Lu, C., and Zhang, S. (2016). Domain Configuration and thermal stability of $(K_{0.48}Na_{0.52})(Nb_{0.96}Sb_{0.04})O_3$-$Bi_{0.50}(Na_{0.82}K_{0.18})_{0.50}ZrO_3$ piezoceramics with high $d_{33}$ coefficient. ACS Appl. Mater. Interfaces *8*, 7257–7265.

Qing, Q., Jiang, Z., Xu, L., Gao, R.X., Mai, L.Q., and Lieber, C.M. (2014). Free-standing kinked nanowire transistor probes for targeted intracellular recording in three dimensions. Nat. Nanotechnol. *9*, 142–147.

Ren, Z., Xu, G., Liu, Y., Wei, X., Zhu, Y., Zhang, X., Lv, G., Wang, Y., Zeng, Y., Du, P., et al. (2010). $PbTiO_3$ nanofibers with edge-shared $TiO_6$ octahedra. J. Am. Chem. Soc. *132*, 5572–5573.

Rim, Y.S., Bae, S.H., Chen, H.J., De Marco, N., and Yang, Y. (2016). Recent progress in materials and devices toward printable and flexible sensors. Adv. Mater. *28*, 4415–4440.

Saito, Y., Takao, H., Tani, T., Nonoyama, T., Takatori, K., Homma, T., Nagaya, T., and Nakamura, M. (2004). Lead-free piezoceramics. Nature *432*, 84–87.

Sun, S.B., Yuan, D., Xu, Y., Wang, A.F., and Deng, Z.T. (2016). Ligand-Mediated synthesis of shape-controlled cesium lead halide perovskite nanocrystals via reprecipitation process at room temperature. ACS Nano *10*, 3648–3657.

Tao, H., and Wu, J. (2016). Giant piezoelectric effect and high strain response in $(1-x)(K_{0.45}Na_{0.55})(Nb_{1-y}Sb_y)O_3$ -$xBi_{0.5}Na_{0.5}Zr_{1-z}Hf_zO_3$ lead-free ceramics. J. Eur. Ceram. Soc. *36*, 1605–1612.

Wang, Z.L. (2018). Nanogenerators, self-powered systems, blue energy, piezotronics and piezo-phototronics - a recall on the original thoughts for coining these fields. Nano Energy *54*, 477–483.

Wang, J.-L., Lu, Y.-R., Li, H.-H., Liu, J.-W., and Yu, S.-H. (2017). Large area co-assembly of nanowires for flexible transparent smart windows. J. Am. Chem. Soc. *139*, 9921–9926.

Wang, X.D., Peng, D.F., Huang, B.L., Pan, C.F., and Wang, Z.L. (2019). Piezophotonic effect based on mechanoluminescent materials for advanced flexible optoelectronic applications. Nano Energy *55*, 389–400.

Wu, J.M., Xu, C., Zhang, Y., Yang, Y., Zhou, Y., and Wang, Z.L. (2012a). Flexible and transparent nanogenerators based on a composite of lead-free $ZnSnO_3$ triangular-belts. Adv. Mater. *24*, 6094–6099.

Wu, J.M., Chen, C.-Y., Zhang, Y., Chen, K.-H., Yang, Y., Hu, Y., He, J.-H., and Wang, Z.L. (2012b). Ultrahigh sensitive piezotronic strain sensors based on a $ZnSnO_3$ nanowire/microwire. ACS Nano *6*, 4369–4374.

Wu, B., Wu, H., Wu, J., Xiao, D., Zhu, J., and Pennycook, S.J. (2016). Giant piezoelectricity and high curie temperature in nanostructured alkali niobate lead-free piezoceramics through phase coexistence. J. Am. Chem. Soc. *138*, 15459–15464.

Xu, S., Yeh, Y.-w., Poirier, G., McAlpine, M.C., Register, R.A., and Yao, N. (2013). Flexible piezoelectric PMN–PT nanowire-based nanocomposite and device. Nano Lett. *13*, 2393–2398.

Xu, K., Li, J., Lv, X., Wu, J.G., Zhang, X.X., Xiao, D.Q., and Zhu, J.G. (2016). Superior piezoelectric properties in potassium-sodium niobate lead-free ceramics. Adv. Mater. *28*, 8519–8523.

Yang, Y., Guo, W., Zhang, Y., Ding, Y., Wang, X., and Wang, Z.L. (2011). Piezotronic effect on the output voltage of P3HT/ZnO micro/nanowire heterojunction solar cells. Nano Lett. *11*, 4812–4817.

Yang, Y., Pradel, K.C., Jing, Q., Wu, J.M., Zhang, F., Zhou, Y., Zhang, Y., and Wang, Z.L. (2012a). Thermoelectric nanogenerators based on single Sb-doped ZnO micro/nanobelts. ACS Nano *6*, 6984–6989.

Yang, Y., Lin, Z.-H., Hou, T., Zhang, F., and Wang, Z.L. (2012b). Nanowire-composite based flexible thermoelectric nanogenerators and self-powered temperature sensors. Nano Res. *5*, 888–895.

Yang, Y., Jung, J.H., Yun, B.K., Zhang, F., Pradel, K.C., Guo, W., and Wang, Z.L. (2012c). Flexible pyroelectric nanogenerators using a composite structure of lead-free KNbO3 nanowires. Adv. Mater. *24*, 5357–5362.

Yang, Y., Lee, J.T., Liyanage, T., and Sardar, R. (2019). Flexible polymer-assisted mesoscale self-assembly of colloidal $CsPbBr_3$ perovskite nanocrystals into higher order superstructures with strong inter-nanocrystal electronic coupling. J. Am. Chem. Soc. *141*, 1526–1536.

You, Y.-M., Liao, W.-Q., Zhao, D., Ye, H.-Y., Zhang, Y., Zhou, Q., Niu, X., Wang, J., Li, P.-F., Fu, D.-W., et al. (2017). An organic-inorganic perovskite ferroelectric with large piezoelectric response. Science *357*, 306–309.

Zang, G.Z., Wang, J.F., Chen, H.C., Su, W.B., Wang, C.M., Qi, P., Ming, B.Q., Du, J., Zheng, L.M., Zhang, S., et al. (2006). Perovskite $(Na_{0.5}K_{0.5})_{1-x}(LiSb)_xNb_{1-x}O_3$ lead-free piezoceramics. Appl. Phys. Lett. *88*, 212908.

Zhai, W., Lin, J., Li, C., Hu, S., Huang, Y., Yu, C., Wen, Z., Liu, Z., Fang, Y., and Tang, C. (2018). Solvothermal synthesis of cesium lead halide perovskite nanowires with ultra-high aspect ratios for high-performance photodetectors. Nanoscale *10*, 21451–21458.

Zhang, Y., Li, L., Bai, W., Shen, B., Zhai, J., and Li, B. (2015). Effect of $CaZrO_3$ on phase structure and electrical properties of KNN-based lead-free ceramics. RSC Adv. *5*, 19647–19651.

Zhang, G.Z., Zhao, P., Zhang, X.S., Han, K., Zhao, T.K., Zhang, Y., Jeong, C.K., Jiang, S.L., Zhang, S.L., and Wang, Q. (2018a). Flexible three-dimensional interconnected piezoelectric ceramic foam based composites for highly efficient concurrent mechanical and thermal energy harvesting. Energy Environ. Sci. *11*, 2046–2056.

Zhang, C., Fan, Y., Li, H., Li, Y., Zhang, L., Cao, S., Kuang, S., Zhao, Y., Chen, A., Zhu, G., et al. (2018b). Fully rollable lead-free poly(vinylidene fluoride)-Niobate-Based nanogenerator with ultra-flexible nano-network electrodes. ACS Nano *12*, 4803–4811.

Zheng, T., Wu, J., Xiao, D., Zhu, J., Wang, X., and Lou, X. (2015). Potassium–sodium niobate lead-free ceramics: modified strain as well as piezoelectricity. J. Mater. Chem. A *3*, 1868–1874.

Zheng, T., Wu, J., Xiao, D., and Zhu, J. (2018). Recent development in lead-free perovskite piezoelectric bulk materials. Prog. Mater. Sci. *98*, 552–624.

Zhou, Q., Park, J.G., Nie, R., Thokchom, A.K., Ha, D., Pan, J., Seok, S.I., and Kim, T. (2018). Nanochannel-assisted perovskite nanowires: from growth mechanisms to photodetector applications. ACS Nano *12*, 8406–8414.

**ISCI, Volume *17***

## Supplemental Information

# Multi-Element Topochemical-Molten Salt Synthesis of One-Dimensional Piezoelectric Perovskite

**Lihong Li, Zhongyuan Xiang, Meng Gao, Cheng Bian, Meng Su, Fengyu Li, Xianran Xing, and Yanlin Song**

## Supplemental Figures

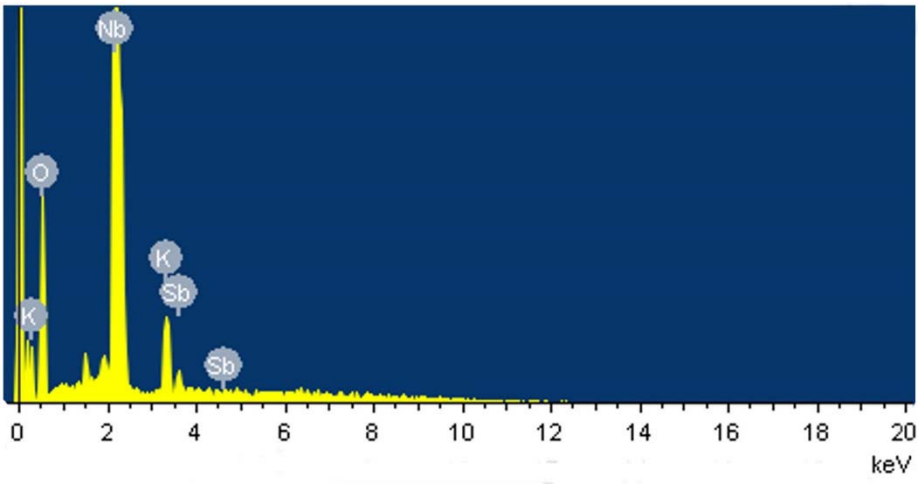


**Figure S1. EDX pattern of non-perovskite-type niobate $K_2(Nb_{0.94}Sb_{0.06})_8O_{21}$ rods with multi-"B-sites", Related to Figure 1**

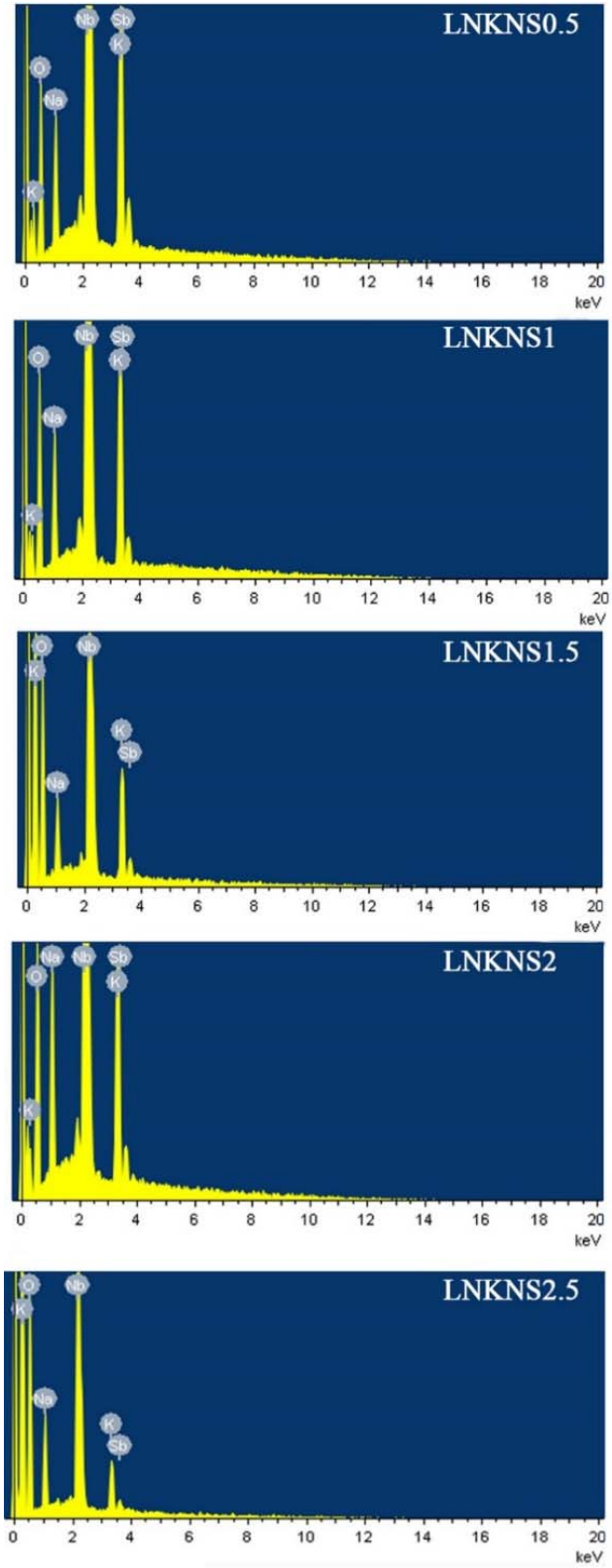


**Figure S2. EDX pattern of perovskite-type niobate LNKNS*m* with different value of *m*（*m*= 0.5, 1, 1.5, 2, and 2.5）, Related to Figures 1, 2**

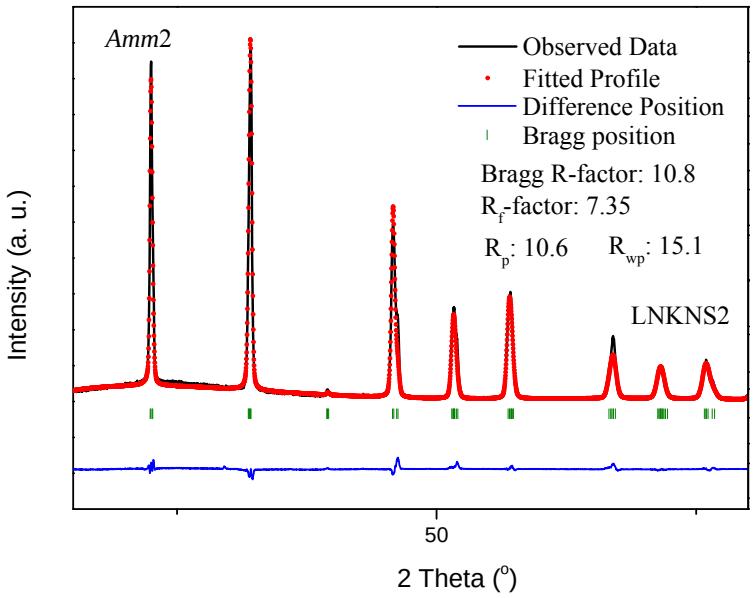


**Figure S3. Rietveld refinement profiles for the 2nd-step synthesized perovskite niobites ($Li_{0.06}Na_{0.47}K_{0.47}$)($Nb_{0.94}Sb_{0.06}$)$O_3$ (LNKNS2). Data were refined in single space group *Amm2*, Related to Figure 2**

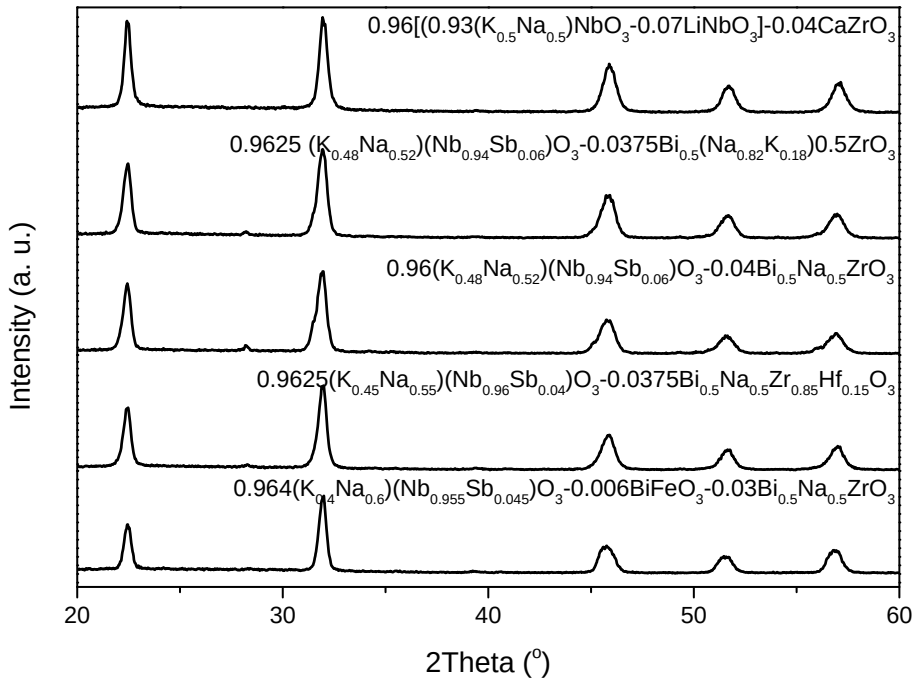


**Figure S4. The XRD patterns of 0.96[(0.93($K_{0.5}Na_{0.5}$)$NbO_3$-0.07$LiNbO_3$]-0.04$CaZrO_3$, 0.9625($K_{0.48}Na_{0.52}$)($Nb_{0.94}Sb_{0.06}$)$O_3$-0.0375$Bi_{0.5}$($Na_{0.82}K_{0.18}$)$_{0.5}ZrO_3$, 0.96($K_{0.48}Na_{0.52}$)($Nb_{0.94}Sb_{0.06}$)$O_3$-0.04$Bi_{0.5}Na_{0.5}ZrO_3$, 0.9625($K_{0.45}Na_{0.55}$)($Nb_{0.96}Sb_{0.04}$)$O_3$-0.0375$Bi_{0.5}Na_{0.5}Zr_{0.85}Hf_{0.15}O_3$ and 0.964($K_{0.4}Na_{0.6}$)($Nb_{0.955}Sb_{0.045}$)$O_3$-0.006$BiFeO_3$-0.03$Bi_{0.5}Na_{0.5}ZrO_3$, Related to Table 1**

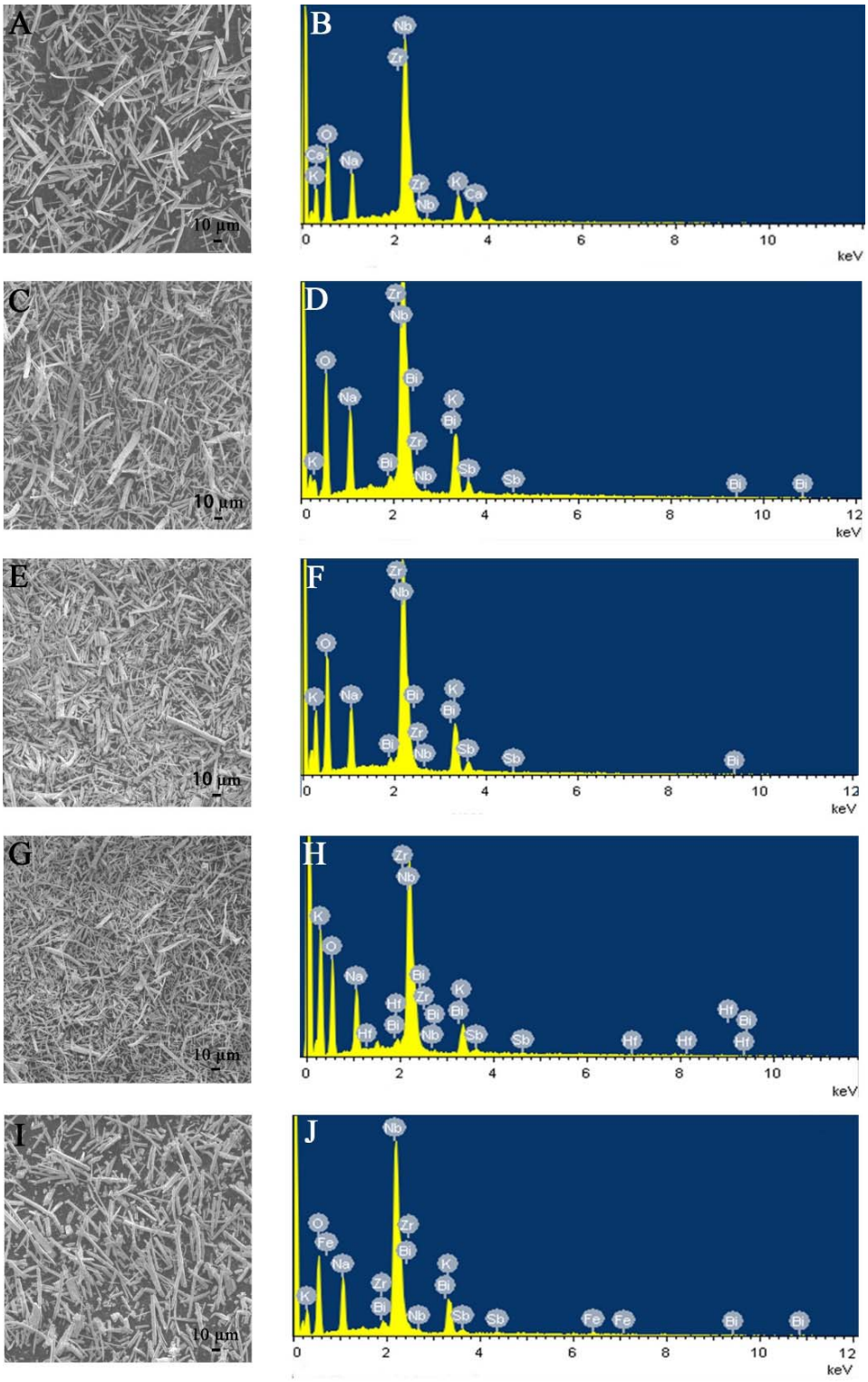


**Figure S5. The SEM and EDX images of the multi-perovskite niobate materials, Related to Table 1**

(A)The SEM and (B) EDX images of 0.96[(0.93($K_{0.5}Na_{0.5}$)$NbO_3$-0.07$LiNbO_3$]-0.04$CaZrO_3$; (C) The SEM and (D) EDX images of 0.9625($K_{0.48}Na_{0.52}$)($Nb_{0.94}Sb_{0.06}$)$O_3$-0.0375$Bi_{0.5}$($Na_{0.82}K_{0.18}$)$_{0.5}ZrO_3$; (E) The SEM and (F) EDX images of 0.96($K_{0.48}Na_{0.52}$)($Nb_{0.94}Sb_{0.06}$)$O_3$-0.04$Bi_{0.5}Na_{0.5}ZrO_3$; (G) The SEM and (H) EDX images of 0.9625($K_{0.45}Na_{0.55}$)($Nb_{0.96}Sb_{0.04}$)$O_3$-0.0375$Bi_{0.5}Na_{0.5}Zr_{0.85}Hf_{0.15}O_3$, and (I) The SEM and (J) EDX images of 0.964($K_{0.4}Na_{0.6}$)($Nb_{0.955}Sb_{0.045}$)$O_3$-0.006$BiFeO_3$-0.03$Bi_{0.5}Na_{0.5}ZrO_3$.

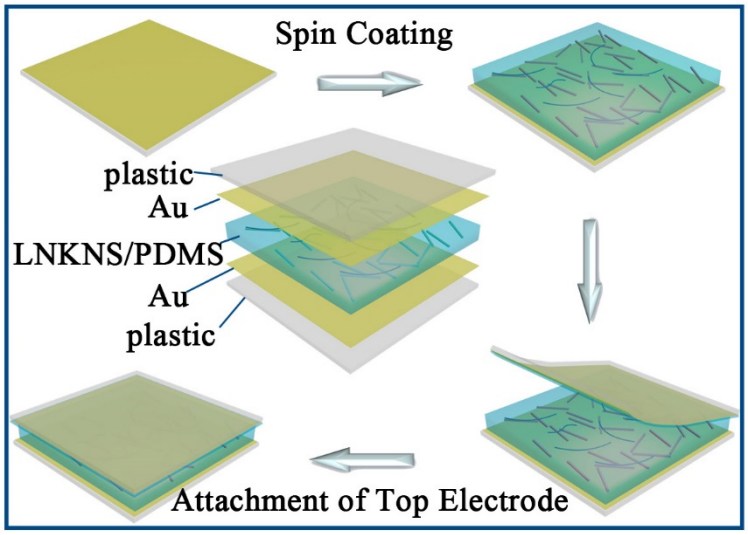


**Figure S6. Schematic illustration of the FPD based on LNKNS2 rods. Briefly, The LNKNS2 rods/PDMS ink was spin-coated onto the bottom electrode. Then, a top electrode was attached to it. In order to orient the electric dipoles in the same direction, an FPD poling was required thereafter, Related to Figure 4**

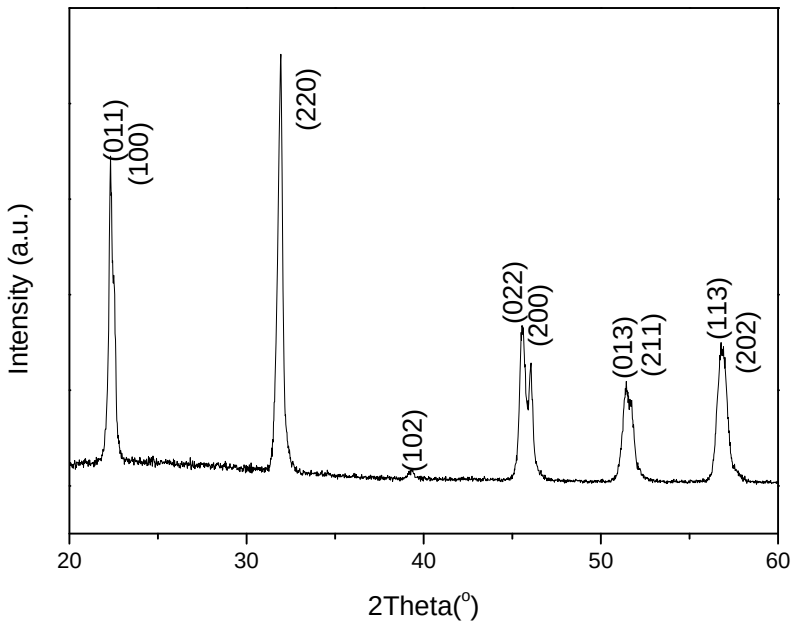


**Figure S7. The XRD pattern of $(Li_{0.06}Na_{0.47}K_{0.47})(Nb_{0.94}Sb_{0.06})O_3$ with morphology of isotropic particles obtained via solid-state method, Related to Figure 4**

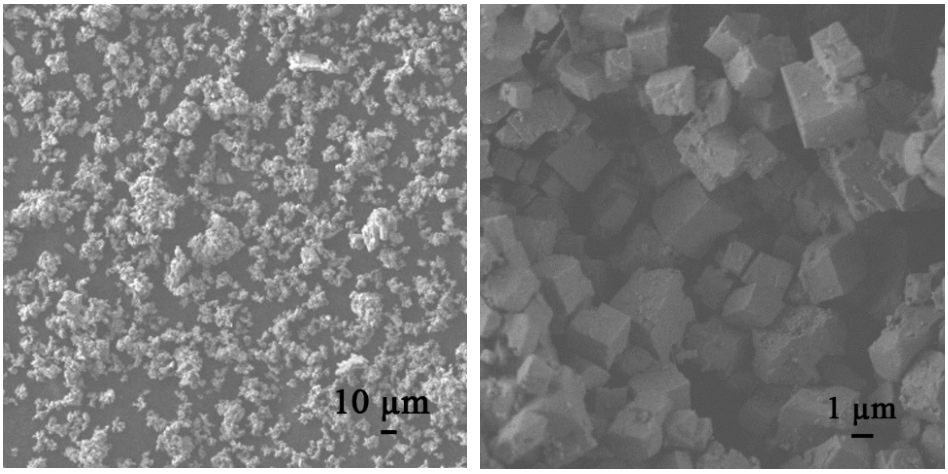


**Figure S8. The SEM images of $(Li_{0.06}Na_{0.47}K_{0.47})(Nb_{0.94}Sb_{0.06})O_3$ (I-LNKNS) isotropic particles obtained via solid-state method. Scale bar: 10 µm and 1 µm, Related to Figure 4**

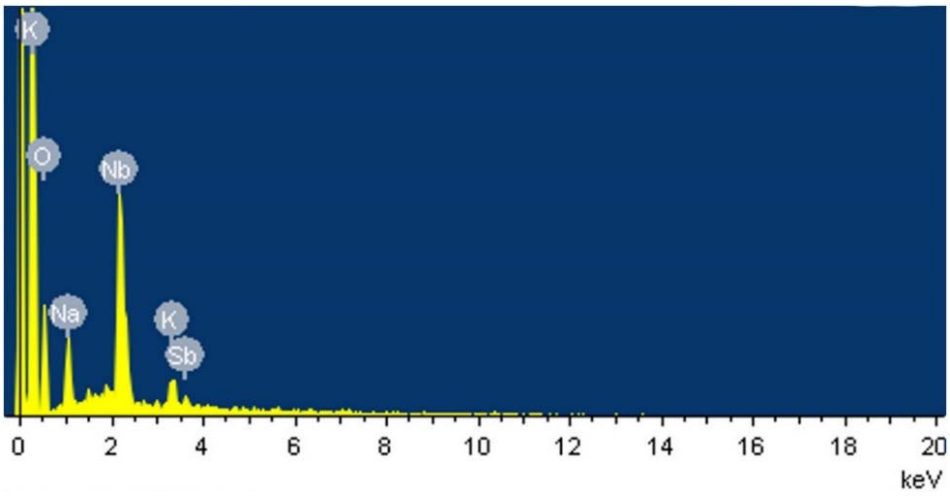


**Figure S9. The EDX pattern of $(Li_{0.06}Na_{0.47}K_{0.47})(Nb_{0.94}Sb_{0.06})O_3$ with morphology of isotropic particles obtained via solid-state method, Related to Figure 4**

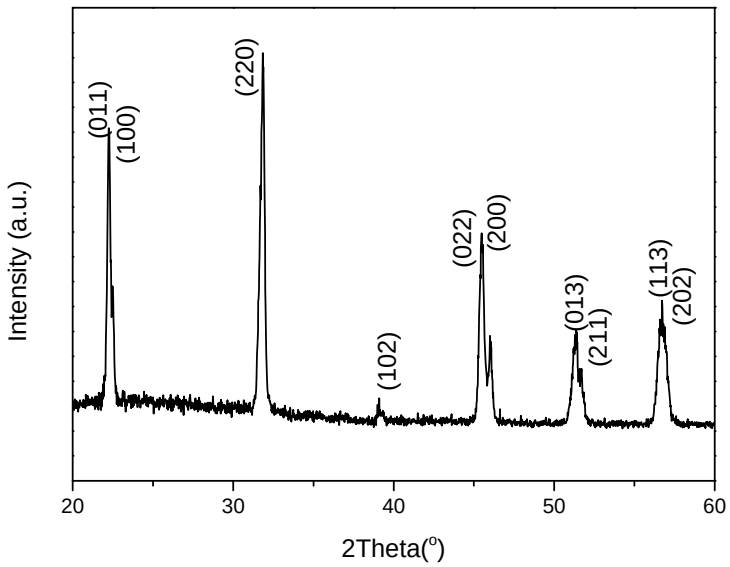


**Figure S10. The XRD pattern of $(Li_{0.06}Na_{0.47}K_{0.47})(Nb_{0.94}Sb_{0.06})O_3$ (S-LNKNS) short rods obtained via MTSS method with small amount of salts, Related to Figure 4**

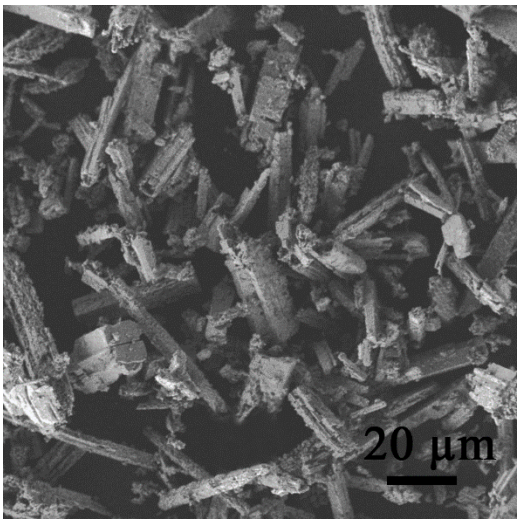


**Figure S11. The SEM images of $(Li_{0.06}Na_{0.47}K_{0.47})(Nb_{0.94}Sb_{0.06})O_3$ (S-LNKNS) short rods obtained via MTSS method with small amount of salts, Related to Figure 4**

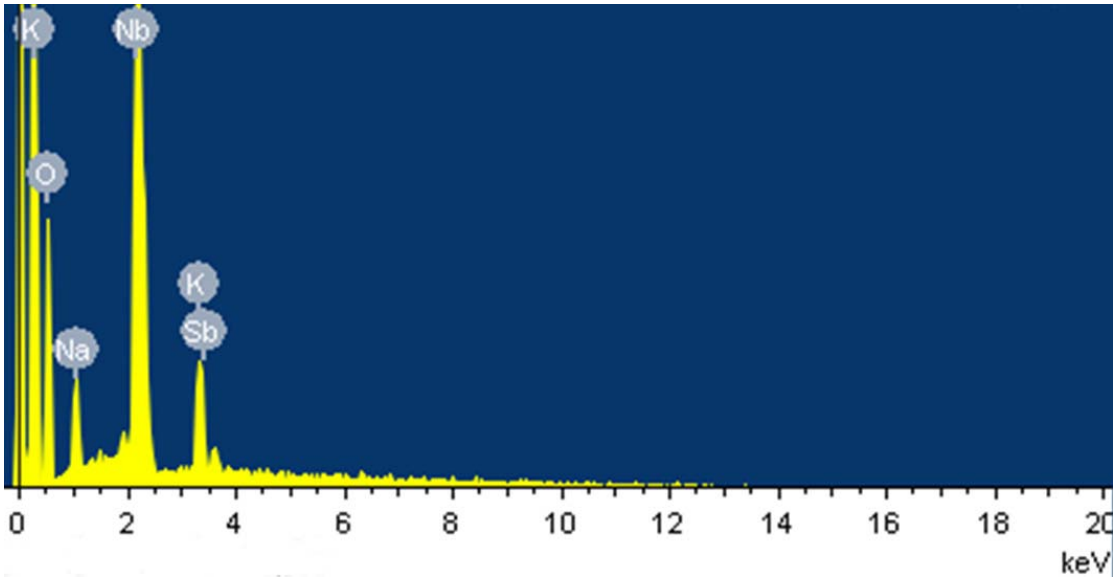


**Figure S12. The EDX pattern of $(Li_{0.06}Na_{0.47}K_{0.47})(Nb_{0.94}Sb_{0.06})O_3$ with morphology of isotropic particles obtained via solid-state method, Related to Figure 4**

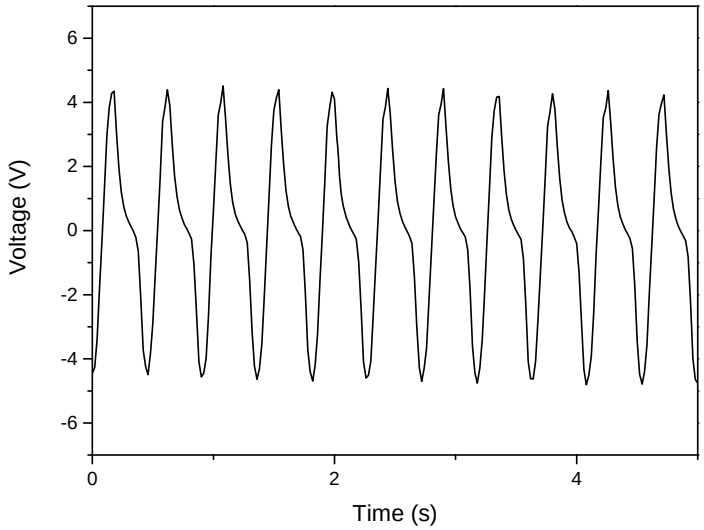


**Figure S13. The open-circuit voltage of S-LNKNS2-FPD measured under the same test condition of LNKNS2-FPD and I-LNKNS-FPD with its bending angle of 120 º, Related to Figure 4**

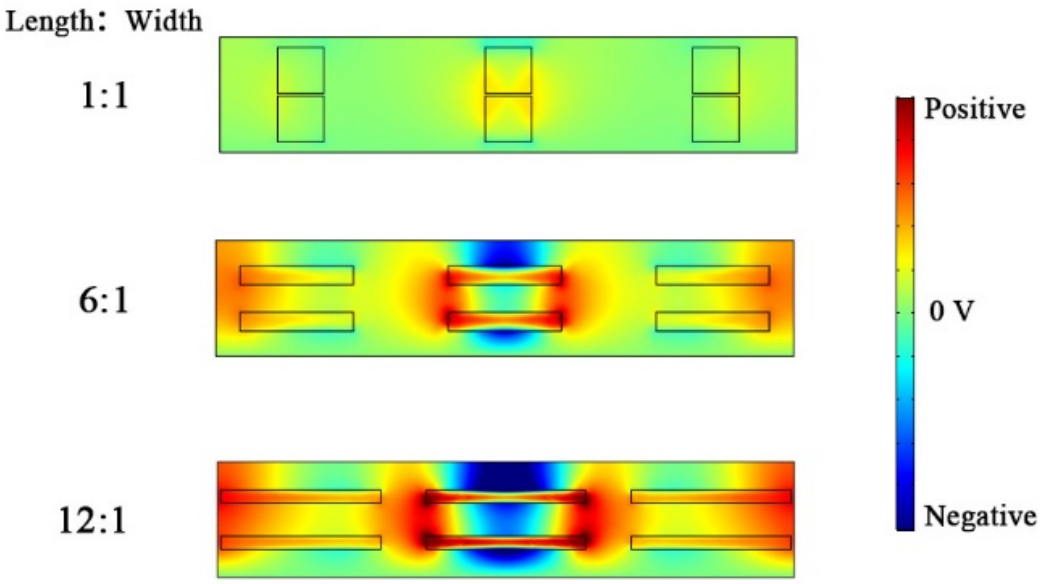


**Figure S14. The simulation of piezoelectric voltage output of the flexible devices with rods of different ratios of length to width (1:1, 1:6, and 1:12), Related to Figure 4**

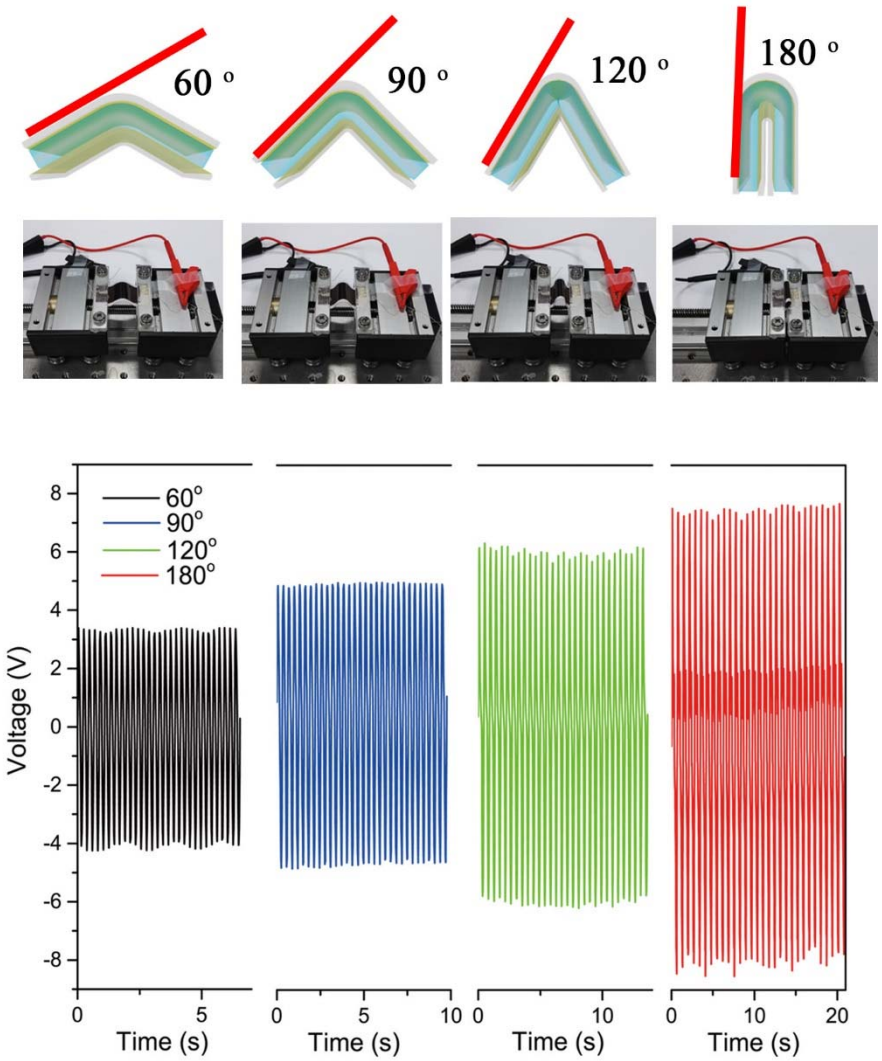


**Figure S15. Optical images of the electricity generation of a LNKNS2-FPD in its different bending states of 60 º, 90 º, 120 º, and 180 º, and the measured open-circuit voltage of a LNKNS2-FPD in its different bending states of 60 º, 90 º, 120 º, and 180 º, Related to Figure 4**

## Supplemental Tables

**Table S1. K/Na/Li/Nb/Sb ratio and the possible formula of LNKNS*m* synthesized by the MTMS method at 850 °C for 100 min with different values of m (amounts of $Na_2CO_3$) [a], Related to Figure 2**

| LNKNS*m* | $K^+$ 0.138 nm [atom-%] | $Na^+$ 0.102 nm [atom-%] | $Li^+$ 0.076 nm [atom-%] | $Nb^{5+}$ 0.064 nm [atom-%] | $Sb^{5+}$ 0.060 nm [atom-%] | Formula |
|---|---|---|---|---|---|---|
| **LNKNS0.5** | 34.2(±0.4) | 12.8(±0.1) | 3.0(±0.1) | 47.1(±0.3) | 2.9(±0.2) | $(K_{0.68}Na_{0.26}Li_{0.06})(Nb_{0.94}Sb_{0.06})O_3$ |
| **LNKNS1** | 29.4(±0.4) | 17.3(±0.1) | 2.9(±0.1) | 47.1(±0.3) | 2.9(±0.2) | $(K_{0.60}Na_{0.34}Li_{0.06})(Nb_{0.94}Sb_{0.06})O_3$ |
| **LNKNS1.5** | 26.0(±0.3) | 21.1(±0.1) | 2.9(±0.1) | 47.2(±0.3) | 2.8(±0.2) | $(K_{0.52}Na_{0.42}Li_{0.06})(Nb_{0.94}Sb_{0.06})O_3$ |
| **LNKNS2** | 23.6(±0.3) | 23.5(±0.1) | 2.9(±0.1) | 47.1(±0.3) | 2.9(±0.2) | $(K_{0.47}Na_{0.47}Li_{0.06})(Nb_{0.94}Sb_{0.06})O_3$ |
| **LNKNS2.5** | 22.4(±0.3) | 24.8(±0.1) | 2.8(±0.1) | 47.0(±0.3) | 3.0(±0.2) | $(K_{0.45}Na_{0.50}Li_{0.06})(Nb_{0.94}Sb_{0.06})O_3$ |

[a] Measured by ICP.

**Table S2. Crystal cell parameters for XRD data of LNKNS*m* with different *m*, Related to Figure 2**

| LNKNS*m* | Symmetry | a (Å) | b (Å) | c (Å) | %Cont [a] |
|---|---|---|---|---|---|
| **LNKNS0.5** | *Amm*2 | 3.956 | 5.653 | 5.653 | 100 |
| **LNKNS1** | *Amm*2 | 3.949 | 5.643 | 5.645 | 100 |
| **LNKNS1.5** | *Amm*2 | 3.939 | 5.630 | 5.626 | 100 |
| **LNKNS2** | *Amm*2 | 3.936 | 5.626 | 5.605 | 80.07 |
| | + *Pmmm* | 3.965 | 3.965 | 3.965 | 19.93 |
| **LNKNS2.5** | *Pmmm* | 3.950 | 3.950 | 3.950 | 100 |

[a] %Cont: percentage of the total integrated intensity

**Table S3. Crystal cell parameters calculated from refinement XRD data of $K_2(Nb_{0.94}Sb_{0.06})_8O_{21}$, Related to Figure 2**

| $K_2(Nb_{0.94}Sb_{0.06})_8O_{21}$ | |
|---|---|
| Orthorhombic, *Pbam* | $\alpha = 90^{o}$ |
| a = 37.4979 Å | $\beta = 90^{o}$ |
| b= 12.5091 Å | $\gamma = 90^{o}$ |
| c= 3.9630 Å | V= 1858.91 $Å^3$ |

**Table S4. Atom parameters calculated from refinement XRD data of $K_2(Nb_{0.94}Sb_{0.06})_8O_{21}$, Related to Figure 2**

| Atom | x | y | z |
|---|---|---|---|
| K1 | 0.16576 | 0.0017 | 0.5 |
| K2 | 0.45421 | 0.36243 | 0.5 |
| K3 | 0.05685 | 0.16928 | 0.5 |
| K4 | 0.22124 | 0.32513 | 0.5 |
| Nb1/ Sb1 | 0.9298 | 0.57263 | 0 |
| Nb2/ Sb2 | 0.89094 | 0.32906 | 0 |
| Nb3/ Sb3 | 0.97687 | 0.29705 | 0 |
| Nb4/ Sb4 | 0.90266 | 0.06989 | 0 |
| Nb5/ Sb5 | 0 | 0 | 0 |
| Nb6/ Sb6 | 0.85708 | 0.79252 | 0 |
| Nb7/ Sb7 | 0.23487 | 0.0719 | 0 |
| Nb8/ Sb8 | 0.16954 | 0.49478 | 0 |
| Nb9/ Sb9 | 0.19217 | 0.78869 | 0 |
| O1 | 0.09993 | 0.3001 | 0 |
| O2 | 0.9817 | 0.60921 | 0 |
| O3 | 0.04869 | 0.57337 | 0 |
| O4 | 0.87682 | 0.49407 | 0 |
| O5 | 0.06967 | 0.78097 | 0 |
| O6 | 0.8732 | 0.91956 | 0 |
| O7 | 0 | 0.16 | 0 |
| O8 | 0.9553 | 0.98875 | 0 |
| O9 | 0.19183 | 0.1355 | 0 |
| O10 | 0.20817 | 0.92974 | 0 |
| O11 | 0.13915 | 0.84897 | 0 |
| O12 | 0.16785 | 0.64003 | 0 |
| O13 | 0.17396 | 0.34925 | 0 |
| O14 | 0.21562 | 0.49897 | 0 |
| O15 | 0.2667 | 0.19893 | 0 |
| O16 | 0.85518 | 0.78064 | 0.5 |
| O17 | 0.92689 | 0.57086 | 0.5 |
| O18 | 0.89129 | 0.32415 | 0.5 |
| O19 | 0.98076 | 0.31584 | 0.5 |
| O20 | 0.89719 | 0.0574 | 0.5 |
| O21 | 0 | 0 | 0.5 |
| O22 | 0.23824 | 0.06696 | 0.5 |
| O23 | 0.17015 | 0.48724 | 0.5 |
| O24 | 0.19023 | 0.7807 | 0.5 |

**Table S5. Crystal cell parameters calculated from refinement XRD data of LNKNS2, Related to Figure 2**

| $(K_{0.47}Na_{0.47}Li_{0.06})(Nb_{0.94}Sb_{0.06})O_3$ (LNKNS2) | Phase No. 1 | Phase No. 2 |
|---|---|---|
| Space group | *Amm2* | *Pmmm* |
| Bragg *R*-factor | 8.07 | 5.03 |
| $R_f$-factor | 5.44 | 2.30 |
| *V* (Å$^3$) | 124.093 | 62.315 |
| a (Å) | 3.9356 | 3.9646 |
| b (Å) | 5.6258 | 3.9646 |
| c (Å) | 5.6047 | 3.9511 |
| α | α = 90 º | α = 90 º |
| β | β = 90 º | β = 90 º |
| γ | γ = 90 º | γ = 90 º |
| ATZ | 1428 | 1428 |
| Brindley | 1.0000 | 1.0000 |
| Fract(%) | 80.07 | 19.93 |

**Table S6. Atom parameters calculated from refinement XRD data of LNKNS2, Related to Figure 2**

| Phase No. 1 | *Amm2* | | |
|---|---|---|---|
| !Atom | X | Y | Z |
| Li | 0 | 0 | 0.27377 |
| Na | 0 | 0 | 0.27377 |
| K | 0 | 0 | 0.27377 |
| Nb | 0.5 | 0 | 0.70324 |
| Sb | 0.5 | 0 | 0.70324 |
| O1 | 0 | 0 | 0.69843 |
| O2 | 0.5 | 0.28114 | 0.90991 |
| Phase No. 2 | *Pmmm* | | |
| !Atom | X | Y | Z |
| Li | 0 | 0 | 0 |
| Na | 0 | 0 | 0 |
| K | 0 | 0 | 0 |
| Nb | 0.5 | 0.5 | 0.5 |
| Sb | 0.5 | 0.5 | 0.5 |
| O1 | 0.5 | 0 | 0.5 |
| O2 | 0.5 | 0.5 | 0 |
| O3 | 0 | 0.5 | 0.5 |

**Table S7. Crystal plane parameters calculated from refinement XRD data of LNKNS2, Related to Figure 2**

| Phase | No. 1 | *Amm2* | | | |
|---|---|---|---|---|---|
| H | K | L | d-hkl | 2theta/TOF | Icalc |
| 0 | 1 | 1 | 3.970564 | 22.372 | 1344.6 |
| 1 | 0 | 0 | 3.935634 | 22.574 | 192.5 |
| 0 | 2 | 0 | 2.812917 | 31.785 | 508.3 |
| 0 | 0 | 2 | 2.802339 | 31.909 | 490 |
| 1 | 1 | 1 | 2.795181 | 31.992 | 1359.6 |
| 1 | 2 | 0 | 2.288483 | 39.338 | 0.8 |
| 1 | 0 | 2 | 2.282777 | 39.441 | 19.7 |
| 0 | 2 | 2 | 1.985282 | 45.66 | 1214.5 |
| 2 | 0 | 0 | 1.967817 | 46.088 | 271.6 |
| 0 | 3 | 1 | 1.778372 | 51.334 | 154.2 |
| 0 | 1 | 3 | 1.773021 | 51.5 | 300.4 |
| 1 | 2 | 2 | 1.772533 | 51.515 | 376.1 |
| 2 | 1 | 1 | 1.76316 | 51.809 | 152 |
| 1 | 3 | 1 | 1.620603 | 56.758 | 535.2 |
| 1 | 1 | 3 | 1.61655 | 56.914 | 361 |
| 2 | 2 | 0 | 1.612428 | 57.072 | 173.3 |
| 2 | 0 | 2 | 1.610428 | 57.15 | 161.2 |
| 0 | 4 | 0 | 1.406458 | 66.415 | 170.4 |
| 0 | 0 | 4 | 1.40117 | 66.698 | 76.1 |
| 2 | 2 | 2 | 1.397591 | 66.892 | 452 |
| 1 | 4 | 0 | 1.324427 | 71.126 | 38.9 |
| 0 | 3 | 3 | 1.323521 | 71.182 | 169.1 |
| 1 | 0 | 4 | 1.320008 | 71.4 | 133.4 |
| 2 | 3 | 1 | 1.319405 | 71.438 | 99 |
| 2 | 1 | 3 | 1.317215 | 71.575 | 189 |
| 3 | 0 | 0 | 1.311878 | 71.911 | 14.7 |
| 0 | 4 | 2 | 1.257024 | 75.582 | 197.3 |
| 1 | 3 | 3 | 1.254485 | 75.762 | 191 |
| 0 | 2 | 4 | 1.254186 | 75.783 | 141.3 |
| 3 | 1 | 1 | 1.245648 | 76.395 | 157.7 |
| Phase | No. 2 | *Pmmm* | | | |
| H | K | L | d-hkl | 2theta/TOF | Icalc |
| 0 | 0 | 1 | 3.94811 | 22.501 | 502.1 |
| 0 | 1 | 0 | 3.94811 | 22.501 | 19.5 |
| 1 | 0 | 0 | 3.94811 | 22.501 | 19.5 |
| 0 | 1 | 1 | 2.791735 | 32.033 | 117.8 |
| 1 | 0 | 1 | 2.791735 | 32.033 | 117.8 |
| 1 | 1 | 0 | 2.791735 | 32.033 | 49 |
| 1 | 1 | 1 | 2.279443 | 39.501 | 0.1 |

| | | | | | |
|---|---|---|---|---|---|
| 0 | 0 | 2 | 1.974055 | 45.934 | 518 |
| 0 | 2 | 0 | 1.974055 | 45.934 | 20.2 |
| 2 | 0 | 0 | 1.974055 | 45.934 | 20.2 |
| 0 | 1 | 2 | 1.765649 | 51.731 | 24.5 |
| 0 | 2 | 1 | 1.765649 | 51.731 | 5.2 |
| 1 | 0 | 2 | 1.765649 | 51.731 | 24.5 |
| 1 | 2 | 0 | 1.765649 | 51.731 | 3.9 |
| 2 | 0 | 1 | 1.765649 | 51.731 | 5.2 |
| 2 | 1 | 0 | 1.765649 | 51.731 | 3.9 |
| 1 | 1 | 2 | 1.611809 | 57.096 | 63.3 |
| 1 | 2 | 1 | 1.611809 | 57.096 | 21.1 |
| 2 | 1 | 1 | 1.611809 | 57.096 | 21.1 |
| 0 | 2 | 2 | 1.395868 | 66.985 | 23.1 |
| 2 | 0 | 2 | 1.395868 | 66.985 | 23.1 |
| 2 | 2 | 0 | 1.395868 | 66.985 | 9.6 |
| 0 | 0 | 3 | 1.316037 | 71.649 | 15.6 |
| 0 | 3 | 0 | 1.316037 | 71.649 | 0.6 |
| 1 | 2 | 2 | 1.316037 | 71.649 | 5.1 |
| 2 | 1 | 2 | 1.316037 | 71.649 | 5.1 |
| 2 | 2 | 1 | 1.316037 | 71.649 | 2.8 |
| 3 | 0 | 0 | 1.316037 | 71.649 | 0.6 |
| 0 | 1 | 3 | 1.248502 | 76.189 | 33.2 |
| 0 | 3 | 1 | 1.248502 | 76.189 | 3.5 |
| 1 | 0 | 3 | 1.248502 | 76.189 | 33.2 |
| 1 | 3 | 0 | 1.248502 | 76.189 | 3 |
| 3 | 0 | 1 | 1.248502 | 76.189 | 3.5 |
| 3 | 1 | 0 | 1.248502 | 76.189 | 3 |

## Transparent Methods

### Chemicals

Niobium pentoxide, antimony trioxide, bismuth trioxide, and ferric oxide were purchased from Sigma-Aldrich. Hafnium oxide was purchased from Innochem. Potassium carbonate, sodium carbonate, lithium carbonate, strontium carbonate, calcium carbonate,potassium chloride and ethanol were purchased from Beijing Chemical Agent Ltd., China. All the materials were used as received without further purification.

### Preparation of 1D rodlike alkaline niobates

Firstly, $K_2(Nb_{0.094}Sb_{0.04})_8O_{21}$ was prepared by molten salt method. $Nb_2O_5$, $Sb_2O_3$ and KCl were mixed in ethanol according to a molar ratio of 0.94:0.04:20. After the mixture was dried at 80 °C, it was transferred to a crucible, loaded into an alumina furnace, and then heated at 1000 °C for 3 h. The product was washed several times with hot deionized water to remove KCl salt. Second, rodlike multi-alkaline niobates $(Li,Na,K)(Nb_{0.094}Sb_{0.06})O_3$, were synthesized from the previously prepared precursors of rodlike $K_2(Nb_{0.094}Sb_{0.06})_8O_{21}$ by the MTMS method. Multi-alkaline niobates of $(Li_{0.06}Na_xK_{0.94-x})(Nb_{0.94}Sb_{0.06})O_3$ was also prepared with the rodlike reactants $K_2(Nb_{0.094}Sb_{0.06})_8O_{21}$, $Li_2CO_3$, and $Na_2CO_3$ in an equal weight of molten salt KCl carried out at 850 °C for 10 min. The molar ratio of the reactants was 0.25:m:0.06 (*m* mol= 0.5, 1, 1.5, 2, and 2.5 mol). The remnant molten salts were removed from the products by washing with hot deionized water several times. The as-synthesized powders were finally dried at 120 °C. This two steps multi-element topo-molten salt method was also applied to achieve other multi-perovskite niobate materials based on the above process.

For the preparation of $0.96[(0.93(K_{0.5}Na_{0.5})NbO_3\text{-}0.07LiNbO_3]\text{-}0.04CaZrO_3$, the raw materials of $Nb_2O_5$, $ZrO_2$, and KCl were firstly mixed in ethanol according to a molar ratio of 0.96:0.04:20. After the mixture was dried at 80 °C, it was transferred to a crucible, loaded into an alumina furnace, and then heated at 1000 °C for 3 h to obtain $K_2(Nb_{0.96}Zr_{0.04})_8O_{21}$. Secondly, the rodlike $K_2(Nb_{0.096}Zr_{0.04})_8O_{21}$, $Li_2CO_3$, $Na_2CO_3$ and $Ca_2CO_3$ were mixed with an equal weight of molten salt KCl carried out at 850 °C for 60 min, and the molar ratio of the reactants was 0.25:0.0672:2:0.04. The remnant molten salts were removed from the product by washing with hot deionized water for several times. The as-synthesized powder was finally dried at 120 °C.

For the preparation of $0.9625(K_{0.48}Na_{0.52})(Nb_{0.94}Sb_{0.06})O_3\text{-}0.0375Bi_{0.5}(Na_{0.82}K_{0.18})_{0.5}ZrO_3$, the raw materials of $Nb_2O_5$, $Sb_2O_3$, $ZrO_2$, and KCl were firstly mixed in ethanol according to a molar ratio of 0.9048:0.0578:0.0375:20. After the mixture was dried at 80 °C, it was transferred to a crucible, loaded into an alumina furnace, and then heated at 1000 °C for 3 h to obtain $K_2((Nb_{0.94}Sb_{0.06})_{0.9625}Zr_{0.0375})_8O_{21}$. Secondly, the rodlike $K_2((Nb_{0.94}Sb_{0.06})_{0.9625}Zr_{0.0375})_8O_{21}$, $Na_2CO_3$, $K_2CO_3$ and $Bi_2O_3$ were mixed with an equal weight of molten salt KCl and reacted at 850 °C for 60 min, and the molar ratio of the reactants was 0.25:2.5:0.0034:0.01875. The remnant molten salts were removed from the product by washing with hot deionized water for several times. The as-synthesized powder was finally dried at 120 °C.

For the preparation of $0.96(K_{0.48}Na_{0.52})(Nb_{0.95}Sb_{0.05})O_3\text{-}0.04Bi_{0.5}Na_{0.5}ZrO_3$, the raw materials of $Nb_2O_5$, $Sb_2O_3$, $ZrO_2$, and KCl were firstly mixed in ethanol according to a molar ratio of 0.912:0.048:0.04:20. After the mixture was dried at 80 °C, it was heated at 1000 °C for 3 h to

obtain $K_2(Nb_{0.0912}Sb_{0.048}Zr_{0.04})_8O_{21}$. Secondly, the rodlike $K_2(Nb_{0.0912}Sb_{0.048}Zr_{0.04})_8O_{21}$, $Na_2CO_3$ and $Bi_2O_3$ were mixed with an equal weight of molten salt KCl and reacted at 850 °C for 60 min, and the molar ratio of the reactants was 0.25:2.5:0.02. After washing and drying, the as-synthesized powder was obtained.

For the preparation of $0.9625(K_{0.45}Na_{0.55})(Nb_{0.96}Sb_{0.04})O_3$-$0.0375Bi_{0.5}Na_{0.5}Zr_{0.85}Hf_{0.15}O_3$, the raw materials of $Nb_2O_5$, $Sb_2O_3$, $ZrO_2$, $HfO_2$ and KCl were firstly mixed in ethanol according to a molar ratio of 0.924:0.037:0.0319:0.00563:20. After the mixture was dried at 80 °C, it was heated at 1000 °C for 3 h to obtain $K_2((Nb_{0.96}Sb_{0.04})_{0.9625}(Zr_{0.85}Hf_{0.15})_{0.0375})_8O_{21}$. Secondly, the rodlike $K_2((Nb_{0.96}Sb_{0.04})_{0.9625}(Zr_{0.85}Hf_{0.15})_{0.0375})_8O_{21}$, $Na_2CO_3$ and $Bi_2O_3$ were mixed with an equal weight of molten salt KCl and reacted at 850 °C for 60 min, and the molar ratio of the reactants was 0.25:3:0.01875. After washing and drying, the as-synthesized powders were obtained.

For the preparation of $0.964(K_{0.4}Na_{0.6})(Nb_{0.955}Sb_{0.045})O_3$-$0.006BiFeO_3$-$0.03Bi_{0.5}Na_{0.5}ZrO_3$, the raw materials of $Nb_2O_5$, $Sb_2O_3$, $Fe_2O_3$, $ZrO_2$, and KCl were firstly mixed in ethanol according to a molar ratio of 0.96:0.04:20. After the mixture was dried at 80 °C, it was transferred to a crucible, loaded into an alumina furnace, and then heated at 1000 °C for 3 h to obtain $K_2(Nb_{0.096}Zr_{0.04})_8O_{21}$. Secondly, the rodlike $K_2(Nb_{0.096}Zr_{0.04})_8O_{21}$, $Li_2CO_3$, $Na_2CO_3$ , $Bi_2O_3$ and $Ca_2CO_3$ were mixed with an equal weight of molten salt KCl carried out at 850 °C for 60 min, and the molar ratio of the reactants was 0.25:0.0672:3.5:0.04. After washing and drying, the as-synthesized powder was obtained.

For the preparation of S-LNKNS, the raw materials of $Nb_2O_5$, $Sb_2O_3$, and KCl were firstly mixed in ethanol according to a molar ratio of 0.96:0.04:5. After the mixture was dried at 80 °C, it was transferred to a crucible, loaded into an alumina furnace, and then heated at 1000 °C for 3 h to obtain $K_2(Nb_{0.96}Sb_{0.04})_8O_{21}$. Secondly, the rodlike $K_2(Nb_{0.096}Sb_{0.04})_8O_{21}$, $Li_2CO_3$, and $Na_2CO_3$ were mixed with an equal weight of molten salt KCl carried out at 850 °C for 10 min, and the molar ratio of the reactants was 0.25:0.06:2. The remnant molten salts were removed from the product by washing with hot deionized water several times. The as-synthesized powder was finally dried at 120 °C.

**Preparation of cubic alkaline niobates**

For comparison, $(Li_{0.06}Na_{0.47}K_{0.47})(Nb_{0.96}Sb_{0.04})O_3$ cubes were prepared by solid-state method. $Nb_2O_5$, $Sb_2O_3$, $Li_2CO_3$, $Na_2CO_3$ and $K_2CO_3$ was mixed in the ratio of 0.94: 0.06: 0.06: 0.47:0.47 in the ethanol, and then heated a furnace at 1080 °C for 10 h after dried at 120 °C.

**FPD fabrication and text**

***Preparation of the piezoelectric composite based ink.*** Piezoelectric nanocomposite-based inks for direct writing and spin coating were prepared by dispersing 40 wt% LNKNS2 rods (or I-LNKNS particles) in PDMS precursor which was the mixture of PDMS base and curing agent in the proportion of 10:1 by weight. The inks were mechanically stirred at 800 rpm for 0.5 h in an icing bath for homogenization.

***Spin coating of the piezoelectric layer.*** The substrate used for spin coating was the bottom electrode, namely an Au/Cr-coated PET film (150 μm in thickness) whose conducting layer was deposited by a high vacuum thermal evaporation system (PATOR, ATT010).The LNKNS2/PDMS (or I-LNKNS /PDMS) ink was spin-coated onto the bottom electrode at the rate of 2000 rpm for 30 s and cured at 120 °C for 1 h.

***FPD fabrication.*** An Au/Cr-coated polyimide film (50 μm in thickness) used as top electrode was attached to the surface of the piezoelectric layer with PDMS precursor served as an adhesive agent. The PDMS adhesive agent was spin-coated onto the top electrode at the rate of 3000 rpm for 30 s and procured at 80 °C for 5 min. After fully hardened at 80 °C for 2 h, the packaged device was poled at 150 °C by applying an electric field for 12 h. The FPDs were poled at 0.8 kV.

***The FPD during the periodic bending/unbending test.*** Employing a bending stage executed at a horizontal displacement of 2 cm with a moving speed of one-side movable fixture of 30 mm/s. This process consisted of cycles of bending and relaxing states. The corresponding power generation mechanism was as follow: in the bending state, the current flow was generated due to dipoles movement from equilibrium position and charges accumulation at two opposite side surfaces of the FPD. In the release state, the accumulated charges returned to their original state, which resulted in output signals in the opposite direction.

**Characterization**

The structure of samples was characterized by X-ray powder diffraction (XRD) patterns, which were obtained on a 21 kW extra power X-ray diffractometer (Rigaku D/MAX 2500) using Cu Kα radiation. The Rietveld refinement of the XRD data with the scanning speed of 2θ angle was $2^{o}$ $min^{-1}$ was calculated via the FULLPROF Suite software. The microstructure of the samples was observed using scanning electron microscopy (SEM, JEOL, JSM-7500, Japan). The composition of powders was determined by energy dispersive X-ray (EDX) analysis with the field-emission scanning electron microscope. The composition of powders was determined by inductively coupled plasma (ICP, INC profile) spectrometry. Transmission electron microscopy (TEM) observation and the corresponding selected area electron diffraction (SAED) patterns were determined with a JEM-1011 TEM, and the samples were prepared by placing a drop of dilute alcohol dispersion of crystals on the surface of a copper grid. The high area transmission electron microscopy (HRTEM) image was taken with a JEM-2100F HRTEM operating at 200 kV accelerating voltage.

**Measuring the piezoelectric property**

Without any special treatment, the as-prepared rod-like LNKNS2 and cubic LNKNS powders were pressed into pellets and then were sintered at 1100 °C for 3 h. The ceramic pellets were polished and coated with silver paste on both sides. Polarization was carried out in a silicon oil bath at 100 °C under applied fields of $E_p$ = 3.5 kV/mm for 20 min. The specimens were cooled to room temperature in the silicon oil bath and then aged for 24 h in air. Then, the piezoelectric coefficient $d_{33}$ of the samples was measured using a quasi-static $d_{33}$ meter (model ZJ-3, Institute of Acoustics, Beijing, China).A bending stage was utilized to apply a periodic deformation to the PNG at a desired displacement and speed. The electrical signal of the PNG device was obtained using a KEITHLEY Model 2450 Interactive SourceMeter Instrument with a HIOKI MR8875-30. The simulation investigation was conducted by using COMSOL multiphysics software.